
A LINDBLAD–PAULI FRAMEWORK FOR COARSE-GRAINED CHAOTIC BINARY-STATE DYNAMICS *

Yicong Qiu

Qiye Zheng[†]

Department of Mechanical and Aerospace Engineering, The Hong Kong University of Science and Technology, Hong Kong

ABSTRACT

Coarse-graining a chaotic bistable oscillator into a binary symbol sequence is a standard and effective reduction, but it often obscures the geometry of the reduced state space and the structural constraints imposed by physically meaningful stochastic evolution. We develop a self-contained two-state framework that embeds the coarse-grained left/right statistics of the driven Duffing oscillator into a 2×2 density-matrix representation and models inter-well switching by a two-rate Gorini–Kossakowski–Sudarshan–Lindblad (GKSL) generator. For diagonal states the GKSL dynamics reduces exactly to the classical two-state master equation. The density-matrix language permits an operational “Bloch half-disk” embedding of phase-space data (with coarse-graining overlap parameter $c(\varepsilon)$ quantifying partition fuzziness); the GKSL model is then fitted to the diagonal marginals (populations) of this embedded state, treating $c(\varepsilon)$ as a diagnostic rather than a dynamical variable. Within this model we derive closed-form solutions for populations and off-diagonal terms, an explicit Kraus representation (generalized amplitude damping composed with dephasing and phase rotation), and practical diagnostics that falsify or support the time-homogeneous first-order Markov assumption from symbol data (order tests, Chapman–Kolmogorov consistency, run-length statistics, and windowed stationarity checks). When diagnostics reveal higher-order memory (e.g., second-order Markov effects), we show how to extend the framework to enlarged state spaces through augmented Markov models, constructing CPTP maps via discrete-time Kraus representations; we note that continuous-time GKSL generators may not exist for all empirical transition matrices. We also provide a detailed numerical-experiment and data-analysis pipeline (with figure/table templates) for validating the framework on Duffing simulations; concrete numerical results are left for a companion computational study. The density-matrix formalism should be viewed as an organizational and algebraic convenience rather than a computational speedup or a claim of quantum-classical equivalence.

Keywords: coarse-graining; Duffing oscillator; two-state master equation; Lindblad (GKSL) dynamics; Kraus representation; Markov diagnostics; generalized probabilistic theories.

1 Introduction

Chaotic bistable oscillators—systems with two stable attractors separated by a basin boundary and driven by periodic forcing or noise—arise in diverse applications including Josephson junctions [1], buckled structures, genetic regulatory networks, and neuronal firing models. When such systems exhibit inter-well transitions on time scales separated from the fast intra-well dynamics, a natural dimensional reduction is to coarse-grain the continuous trajectory into a discrete binary symbol sequence: “left” vs. “right” well occupancy. This symbolic encoding has proven effective in analyzing chaos [2], stochastic resonance [3, 4], and rare-event transitions in complex systems.

However, standard symbolic dynamics and empirical two-state rate equations face three persistent challenges. First, **coarse-graining ambiguity** is typically left implicit: the choice of partition boundary and its effect on inferred

Citation:* Y. Qiu and Q. Zheng, **A Lindblad–Pauli Framework for Coarse-Grained Chaotic Binary-State Dynamics. arXiv preprint (2025).

[†]Corresponding author: qiyezheng@ust.hk

transition rates are rarely quantified systematically. Most implementations adopt a hard partition (e.g., $\text{sign}(x)$) and assume that boundary effects are negligible, without providing a measurable diagnostic for when this assumption holds. Second, **Markov closure is often assumed without validation**: discrete-time or continuous-time Markov models are fitted directly to symbol sequences, yet the first-order Markov property (memorylessness) is rarely tested explicitly; higher-order memory effects, time-inhomogeneity, or hidden variables can invalidate these models, leading to spurious rate estimates and unreliable predictions. Third, **model extensions lack systematic guarantees**: when the Markov assumption fails (e.g., due to memory of the previous two states), ad hoc extensions are constructed without ensuring that the resulting dynamics remain completely positive and trace-preserving (CPTP)—requirements that are trivial for classical probability vectors but subtle when off-diagonal correlations or soft-partition overlaps are present.

In this work, we develop a unified framework that addresses these challenges by embedding coarse-grained binary statistics into the mathematical structure of quantum two-level systems, while emphasizing that this is a *representational tool* rather than a claim of quantum behavior in classical dynamics. The Gorini–Kossakowski–Sudarshan–Lindblad (GKSL) theorem [5, 6, 7] provides a complete characterization of Markovian CPTP generators in finite dimension; classical two-state master equations are recovered exactly as the diagonal restriction of GKSL dynamics. The density-matrix language organizes coarse-grained statistics into a 2×2 Hermitian matrix with unit trace, where diagonal entries encode occupation probabilities and the off-diagonal entry quantifies partition overlap or measurement uncertainty. This embedding is not new in principle—classical probability vectors can always be embedded into diagonal density matrices—but the systematic operational implementation for chaotic bistable systems, including explicit soft partitions, falsifiable diagnostics, and CPTP-preserving extensions, has not been developed.

Our approach distinguishes between two density matrices: $\rho_{\text{emb}}(t)$, the *embedded state* constructed directly from phase-space data via soft-partition membership weights $w_L(z)$, $w_R(z)$ (with tunable fuzziness parameter ε), and $\rho_{\text{mod}}(t)$, the *model state* that evolves under a two-rate GKSL generator fitted to the diagonal marginals (populations p_L , p_R) extracted from ρ_{emb} . The overlap parameter $c(\varepsilon) = \langle \sqrt{w_L w_R} \rangle$ quantifies boundary fuzziness but is *not* a dynamical variable of the reduced model; it serves as a coarse-graining diagnostic. The GKSL model governs only population evolution from symbol observations; off-diagonal coherences in ρ_{mod} represent initial-state uncertainty or mixed preparations and decay to zero at steady state, consistent with the fact that symbols provide no boundary-proximity information.

The primary motivation for adopting GKSL formalism is **mathematical consistency and automatic CPTP guarantees**: any Markovian dynamics on a two-state system that preserves normalization and nonnegativity of probabilities can be represented in GKSL form (or its discrete-time Kraus counterpart), ensuring that model extensions remain physically consistent by construction. This is particularly valuable when diagnostics reject the first-order Markov assumption and state-space augmentation is required (e.g., second-order Markov effects necessitate a four-state model on symbol pairs). Classical rate-equation extensions require manual verification of positivity and normalization constraints at each step; GKSL/Kraus representations inherit these guarantees from the operator-algebraic structure. We emphasize that this is an *organizational and algebraic* convenience, not a computational speedup: for classical measurement records, classical matrix exponentiation remains the efficient implementation route.

1.1 Related work and positioning

Two-state reductions of bistable systems have a long history in nonlinear dynamics and statistical physics. In the stochastic resonance literature [3, 4], continuous double-well systems are approximated by two-state master equations with effective switching rates derived from barrier heights, forcing amplitude, and noise intensity via Kramers theory or numerical fitting. For deterministic chaotic bistability (e.g., the driven Duffing oscillator), a two-state description is an empirical reduction whose adequacy depends on sampling time scale and memory effects. Our framework differs in three respects: (i) we provide an explicit soft-partition map with quantifiable overlap $c(\varepsilon)$, making coarse-graining resolution testable; (ii) we supply falsifiable diagnostics (order tests, Chapman–Kolmogorov consistency, run-length analysis) with explicit rejection criteria; (iii) we derive closed-form analytical solutions and an equivalence to generalized amplitude damping Kraus operators, connecting the model to quantum-information-theoretic representations.

On the quantum side, the GKSL theorem is foundational for open quantum system dynamics [5, 6, 7]. Recent extensions include universal Lindblad equations [8], dissipative quantum chaos [9, 10], many-body systems via Lieb–Robinson bounds [11], and classical-quantum correspondence [12, 13, 14]. Quantum stochastic walks [15] use GKSL-type interpolation between classical and coherent dynamics on graphs. Quantum simulation of chaotic systems [16, 17] explores quantum trajectories and superpositions at the microscopic level. Our framework differs fundamentally in scope: we focus on *classical observables* (left/right occupancy, switching rates, run-length statistics) from deterministic or noise-driven trajectories, using density matrices as an organizational structure for coarse-grained statistics. The connection between density-matrix methods and phase-space dynamics has been explored via Koopman operator

theory [18, 19, 20] and generalized probabilistic theories [21, 22], which provide the mathematical foundation for convex-geometric state-space representations without requiring quantum superposition at the physical level.

1.2 Contributions and paper organization

While the formal equivalence between diagonal GKSL dynamics and classical two-state Markov processes is well established, this work provides three operational contributions. First, we present a **testable geometric embedding with quantified coarse-graining ambiguity**. We derive a soft-partition map (Definition 3.1) that constructs ρ_{emb} from phase-space data with explicit overlap parameter $c(\varepsilon)$, where ε controls boundary width. The embedding satisfies three independent consistency criteria: (a) information-geometric isometry for diagonal states [23, 24], (b) automatic positivity via Cauchy–Schwarz, (c) operational interpretation as the Bhattacharyya coefficient. The resulting Bloch half-disk geometry (Theorem 3.2) imposes the constraint $c^2 \leq p_L p_R$, making partition ambiguity explicit and measurable. This allows systematic selection of ε by minimizing c , matching empirical purity, or requiring $c^2 \ll p_L p_R$ (near-classical limit).

Second, we develop a **falsifiable diagnostic pipeline with explicit rejection criteria**. We present four complementary tests (Section 4): (a) order tests comparing first- vs. second-order Markov log-likelihoods via G-test with χ^2 asymptotics; (b) Chapman–Kolmogorov consistency $\|\hat{\mathbf{P}}^{(2)} - \hat{\mathbf{P}}^2\|_F$ with bootstrap confidence intervals; (c) run-length histograms testing memorylessness via geometric-distribution fits; (d) windowed stationarity with confidence-interval overlap and heterogeneity χ^2 tests. Each test makes falsifiable predictions (e.g., $\hat{\mathbf{P}}^{(2)} \approx \hat{\mathbf{P}}^2$ for Markov closure, geometric run-length distributions for memorylessness). Practical guidance for sparse counts (permutation tests, pseudocount smoothing) and stationarity thresholds (Wald intervals, change-point detection) ensures robust application to finite datasets.

Third, we provide **analytical results and CPTP-preserving extensions**. We derive closed-form evolution equations (Section 3.1), exact solutions for populations and coherences (Section 3.2), discrete-time Poincaré-map formulations with rate-inversion formulas (Section 3.3), and an explicit Kraus representation proving equivalence to generalized amplitude damping composed with dephasing and phase rotation (Section 3.4). When diagnostics reject first-order Markov closure, we provide systematic state-space augmentation protocols (Section 4.5) that preserve CPTP guarantees by construction; we also give practical criteria for assessing whether continuous-time GKSL generators exist (eigenvalue positivity, matrix-logarithm rate extraction, semigroup consistency) or whether discrete-time Kraus operators should be used instead.

The paper is organized as follows. Section 2 describes the driven Duffing oscillator, Poincaré sampling, binary symbol generation, soft-partition membership functions, and the two-rate GKSL model (our methodological setup). Section 3 presents analytical results: evolution equations, closed-form solutions, steady-state characterization, discrete-time formulation, and Kraus representation with equivalence proof. Section 4 develops the diagnostic framework: order tests, Chapman–Kolmogorov consistency, run-length analysis, windowed stationarity, and model-extension protocols. Section 5 outlines numerical methods and computational validation procedures; detailed figure/table templates are provided in Appendices. Section 6 discusses scope, limitations, interpretive caveats (the two-matrix distinction ρ_{emb} vs. ρ_{mod} , embedding problem for higher-order extensions, relationship to Koopman methods), and future directions. Section 7 concludes. Appendices contain derivation details, the complete Kraus equivalence proof, discussion of why pure Hamiltonian evolution cannot model switching, symmetry considerations, a summary of key formulas, and a comprehensive notation reference (Appendix F).

2 Methods: Model setup

2.1 Driven Duffing oscillator

We consider the driven, damped Duffing oscillator

$$\ddot{x} + \delta \dot{x} - \alpha x + \beta x^3 = \gamma_0 \cos(\omega t), \quad (1)$$

where x is displacement, $\delta > 0$ is damping, $\alpha > 0$ and $\beta > 0$ define a symmetric double-well potential, γ_0 is forcing amplitude, and ω is forcing frequency. The potential energy is

$$V(x) = -\frac{1}{2}\alpha x^2 + \frac{1}{4}\beta x^4, \quad (2)$$

with stable equilibria at $x_{\pm} = \pm\sqrt{\alpha/\beta}$ and barrier height $\Delta V = \alpha^2/(4\beta)$.

Remark 2.1 (Optional stochastic extension). If one adds Gaussian white noise $\sqrt{2D}\xi(t)$ to the forcing, the switching statistics often become closer to Poisson at suitable sampling scales, which can strengthen the empirical case for a time-homogeneous Markov reduction:

$$\ddot{x} + \delta\dot{x} - \alpha x + \beta x^3 = \gamma_0 \cos(\omega t) + \sqrt{2D}\xi(t). \quad (3)$$

The deterministic ($D = 0$) development below still applies; the noise term simply changes the effective rates and can broaden the boundary region, which can be modeled by the soft-partition parameter ε (Section 2.3).

2.2 Poincaré sampling and symbol sequence

Let $T = 2\pi/\omega$ be the forcing period, and define sampling times $t_n = nT$. The simplest binary coding uses the sign of $x(t_n)$:

Definition 2.2 (Binary symbol sequence). Define $S_n \in \{L, R\}$ by

$$S_n = \begin{cases} L, & x(t_n) < 0, \\ R, & x(t_n) > 0. \end{cases} \quad (4)$$

This yields a discrete-time binary process $\{S_n\}_{n \geq 0}$ (after discarding transients).

In practice, one may use more refined boundary functions than $x \mapsto \text{sign}(x)$ (for instance, an approximate separatrix on the stroboscopic section), and one may also consider windowed statistics (e.g. average over $t \in [t_n, t_n + \Delta]$) rather than pointwise sampling. Figure 2 illustrates an example segment of the resulting binary symbol sequence.

2.3 Soft-partition embedding and Bloch geometry

To quantify the effect of coarse-graining resolution on the reduced statistics, we now formalize the embedding of phase-space data into a 2×2 density matrix with an explicit overlap parameter $c(\varepsilon)$ that characterizes boundary fuzziness.

2.3.1 Two-state basis and Pauli operators

We introduce the computational basis

$$|L\rangle = \begin{pmatrix} 1 \\ 0 \end{pmatrix}, \quad |R\rangle = \begin{pmatrix} 0 \\ 1 \end{pmatrix}, \quad (5)$$

together with the Pauli matrices

$$\sigma_x = \begin{pmatrix} 0 & 1 \\ 1 & 0 \end{pmatrix}, \quad \sigma_y = \begin{pmatrix} 0 & -i \\ i & 0 \end{pmatrix}, \quad \sigma_z = \begin{pmatrix} 1 & 0 \\ 0 & -1 \end{pmatrix}. \quad (6)$$

We also use the raising/lowering operators

$$\sigma_+ = |R\rangle\langle L| = \begin{pmatrix} 0 & 0 \\ 1 & 0 \end{pmatrix}, \quad \sigma_- = |L\rangle\langle R| = \begin{pmatrix} 0 & 1 \\ 0 & 0 \end{pmatrix}. \quad (7)$$

2.4 Density matrices and the Bloch representation

A (qubit) density matrix ρ is a 2×2 Hermitian positive semidefinite matrix with unit trace. Equivalently, any such ρ can be written in Bloch form

$$\rho = \frac{1}{2} \left(\mathbb{I} + m_x \sigma_x + m_y \sigma_y + m_z \sigma_z \right) = \frac{1}{2} \begin{pmatrix} 1 + m_z & m_x - im_y \\ m_x + im_y & 1 - m_z \end{pmatrix}, \quad (8)$$

with Bloch vector $\mathbf{m} = (m_x, m_y, m_z)$ satisfying $\|\mathbf{m}\| \leq 1$.

Remark 2.3 (Classical diagonal states). A purely classical two-state distribution (p_L, p_R) corresponds to a diagonal density matrix

$$\rho = \begin{pmatrix} p_L & 0 \\ 0 & p_R \end{pmatrix} = \frac{1}{2} (\mathbb{I} + m_z \sigma_z), \quad m_z = p_L - p_R. \quad (9)$$

In this case only m_z is needed.

2.5 Soft partitions and an operational overlap parameter

Why introduce off-diagonal terms? A single deterministic Duffing trajectory is never “in a superposition” of wells. However, a *coarse-grained* description may be uncertain when the trajectory is close to the boundary or when observations are aggregated over a finite window. We represent this uncertainty by soft membership functions and an embedding that produces a real-symmetric 2×2 matrix with a nonnegative off-diagonal entry.

Definition 2.4 (Soft partition / membership functions). Let $z = (x, \dot{x})$ denote a point on a chosen Poincaré section. Introduce $w_L(z) \in [0, 1]$ and $w_R(z) = 1 - w_L(z)$ with

$$w_L(z) = \frac{1}{2} \left(1 - \tanh\left(\frac{g(z)}{\varepsilon}\right) \right), \quad w_R(z) = \frac{1}{2} \left(1 + \tanh\left(\frac{g(z)}{\varepsilon}\right) \right), \quad (10)$$

where $g(z)$ is a signed boundary function (zero level-set approximates the separatrix on the section) and $\varepsilon > 0$ controls fuzziness. The hard partition is recovered as $\varepsilon \rightarrow 0^+$. For exposition we often take $g(z) = x$.

Definition 2.5 (Pointwise embedded two-state vector). Associate to each z the real-amplitude vector

$$|\psi(z)\rangle = \sqrt{w_L(z)} |L\rangle + \sqrt{w_R(z)} |R\rangle. \quad (11)$$

This is an embedding device that encodes partial membership induced by coarse-graining; it is not a microscopic quantum state of the Duffing oscillator.

Remark 2.6 (Why the square-root embedding?). The choice of square-root weighting in (11) is not arbitrary but is motivated by three independent considerations from information geometry, positivity constraints, and statistical overlap measures.

(1) Hellinger distance and information geometry. The Hellinger distance between probability distributions p and q is $H(p, q) = \sqrt{1 - \int \sqrt{p(x)q(x)} dx}$. The square-root embedding connects the Bloch-sphere geometry to the Fisher-Rao information geometry for the classical (diagonal/commuting) submanifold [23, 24], establishing a close connection between the Fubini-Study metric and the Fisher-Rao metric for this restricted case. This ensures that geometric notions (distance, curvature) have consistent interpretations across quantum and classical descriptions.

(2) Automatic positivity via Cauchy-Schwarz. With the square-root embedding, the off-diagonal element $c(t) = \int \mu_t(z) \sqrt{w_L(z)w_R(z)} dz$ satisfies $c^2 \leq p_L p_R$ by the Cauchy-Schwarz inequality applied to $\int \sqrt{w_L} \sqrt{w_R}$. This *automatically* ensures that the resulting density matrix is positive semidefinite without additional constraints. Alternative embeddings (e.g., $c = \int w_L w_R$ or $c = \int w_L^{1/3} w_R^{2/3}$) would require manual verification of positivity at each time step.

(3) Bhattacharyya overlap coefficient. Define induced sub-densities $p_L(z) = \mu_t(z)w_L(z)$ and $p_R(z) = \mu_t(z)w_R(z)$. Then

$$c(t) = \int \sqrt{p_L(z)p_R(z)} dz$$

is precisely the Bhattacharyya coefficient (Hellinger affinity) between p_L and p_R [25]. This standard measure of distributional overlap in statistics and pattern recognition gives $c(t)$ a direct operational interpretation: it quantifies the overlap between left-well and right-well membership distributions at resolution ε .

These three principles—information-geometric isometry, automatic positivity, and statistical interpretability—converge to the same embedding, demonstrating that the square-root choice is principled rather than ad hoc. Alternative embeddings are possible (e.g., direct diagonal: $\rho = \text{diag}(p_L, p_R)$ with $c = 0$), but forfeit either geometric naturalness or the ability to represent partition fuzziness.

Definition 2.7 (Ensemble or window-reduced state). Let $\mu_t(z)$ be a probability density (e.g. an ensemble of initial conditions) or an empirical measure derived from a time window. Define the embedded state

$$\rho_{\text{emb}}(t; \varepsilon, \Delta) = \int \mu_t(z) |\psi(z)\rangle \langle \psi(z)| dz. \quad (12)$$

Proposition 2.8 (Matrix elements and overlap). With $\rho_{\text{emb}}(t; \varepsilon, \Delta)$ as in (12),

$$[\rho_{\text{emb}}]_{LL}(t) = \int \mu_t(z) w_L(z) dz =: p_L(t), \quad (13)$$

$$[\rho_{\text{emb}}]_{RR}(t) = \int \mu_t(z) w_R(z) dz =: p_R(t) = 1 - p_L(t), \quad (14)$$

$$[\rho_{\text{emb}}]_{LR}(t) = \int \mu_t(z) \sqrt{w_L(z)w_R(z)} dz =: c(t) \in [0, \frac{1}{2}]. \quad (15)$$

The upper bound $c(t) \leq \frac{1}{2}$ follows from the constraint $w_L + w_R = 1$ and the AM-GM inequality: $\sqrt{w_L w_R} \leq \frac{w_L + w_R}{2} = \frac{1}{2}$, with equality only when $w_L = w_R = \frac{1}{2}$ (maximum boundary fuzziness). Thus

$$\rho_{\text{emb}}(t) = \begin{pmatrix} p_L(t) & c(t) \\ c(t) & 1 - p_L(t) \end{pmatrix}. \quad (16)$$

Moreover $c(t) \rightarrow 0$ in the hard-partition limit $\varepsilon \rightarrow 0^+$.

Definition 2.9 (Windowed empirical measure). Given a trajectory $z(t)$ on the section and a window length $\Delta > 0$, define

$$\mu_{t,\Delta}(A) = \frac{1}{\Delta} \int_t^{t+\Delta} \mathbf{1}_{\{z(s) \in A\}} ds \quad (17)$$

for measurable sets A .

Remark 2.10 (Discrete Poincaré sampling). For discrete Poincaré samples $z_n = z(t_n)$ with $t_n = nT$, the windowed measure becomes

$$\mu_{n,M}(A) = \frac{1}{M} \sum_{j=0}^{M-1} \mathbf{1}_{\{z_{n+j} \in A\}},$$

where M is the window length in sampling periods.

Remark 2.11 (Operational meaning of $c(t)$). Under the windowed measure $\mu_{t,\Delta}$, $c(t; \Delta)$ increases when the window overlaps the inter-well boundary region where $w_L w_R > 0$. Thus $c(t)$ quantifies *how much of the coarse-grained mass is near the decision boundary*. In empirical work, one may estimate c from sampled points by

$$\hat{c} = \frac{1}{N} \sum_{n=1}^N \sqrt{w_L(z(t_n)) w_R(z(t_n))},$$

with w_L, w_R fixed by the chosen coarse-graining and resolution parameter ε .

Remark 2.12 ($c(t)$ is not a dynamical variable). The overlap parameter $c(t)$ characterizes the coarse-graining resolution but is *not* a dynamical observable of the reduced model. The GKSL model (Section 2.7) governs the evolution of populations $p_L(t), p_R(t)$ from symbol observations; the off-diagonal entries ρ_{LR} in the density-matrix representation encode initial-state uncertainty or measurement resolution, but cannot be inferred from symbol data alone. In practice, $c(\varepsilon)$ serves as a diagnostic for partition quality: smaller c indicates sharper boundaries and better approximation of the classical limit (diagonal states). The GKSL steady state ρ^* is diagonal (Theorem 3.4), which is consistent because symbols provide no boundary-proximity information.

Two density matrices: embedding vs. dynamical model. We distinguish two density-matrix objects throughout this work. The first is the *embedded state* $\rho_{\text{emb}}(t; \varepsilon, \Delta)$ constructed from phase-space data via the soft-partition map (11) and (12). This state is a functional of the phase-space distribution $\mu_t(z)$ and the partition parameters (ε, Δ) ; its off-diagonal element $[\rho_{\text{emb}}]_{LR} = c(t; \varepsilon)$ quantifies boundary overlap and serves as a coarse-graining diagnostic. The second is the *model state* $\rho_{\text{mod}}(t)$ governed by the GKSL equation (Section 2.7). This state represents the reduced two-state dynamics inferred from symbol observations $\{S_n\}$. In practice, the GKSL model is fitted and validated against the *diagonal marginals* of ρ_{emb} , namely the populations $p_L(t), p_R(t)$. The off-diagonal terms of ρ_{mod} represent initial-state uncertainty or mixed preparations; they are not directly measurable from symbol data and decay to zero at steady state (Theorem 3.4).

The overlap parameter $c(t; \varepsilon)$ characterizes the quality of the coarse-graining (how much boundary region is ambiguous) but is *not* a closed dynamical variable of ρ_{mod} . The two-state GKSL framework models population evolution from symbols; boundary-proximity information in $c(\varepsilon)$ requires phase-space or soft-membership data beyond the symbol sequence.

2.6 Bloch half-disk geometry

Theorem 2.13 (Bloch half-disk state space). *A real-symmetric matrix of the form (16) (i.e., ρ_{emb} with off-diagonal $c(t)$) is positive semidefinite if and only if*

$$c(t)^2 \leq p_L(t)(1 - p_L(t)). \quad (18)$$

Equivalently, writing $\rho_{\text{emb}} = \frac{1}{2}(\mathbb{I} + m_x \sigma_x + m_z \sigma_z)$ with $m_y = 0$, one has $m_x = 2c \geq 0$ and

$$\mathcal{S}_{\text{half-disk}} = \left\{ \rho : m_y = 0, m_x \geq 0, m_x^2 + m_z^2 \leq 1 \right\}. \quad (19)$$

The classical two-state simplex corresponds to the diameter $m_x = 0$ (diagonal states).

Proof. For $\rho = \begin{pmatrix} p & c \\ c & 1-p \end{pmatrix}$, $\text{Tr}(\rho) = 1$ and $\det(\rho) = p(1-p) - c^2$. Positive semidefiniteness is equivalent to $\det(\rho) \geq 0$, yielding (18). Using $m_z = 2p - 1$ and $m_x = 2c$ gives $m_x^2 + m_z^2 \leq 1$ with $m_y = 0$. Nonnegativity of c follows from the integral definition in Proposition 2.8. \square

Remark 2.14 (State-space geometry vs accessible measurements). The half-disk describes the *embedded state space*. If the only accessible readout is L/R occupancy (a σ_z -type measurement), then states with the same p_L are operationally indistinguishable. To operationalize $c(t)$ one must define additional observables tied to the boundary region (e.g. short-time boundary-crossing indicators or augmented coarse-grainings).

Remark 2.15 (Closure of the half-disk). The half-disk state space is closed under evolution only when $\Omega = 0$ (no energy splitting) and initial states are real-symmetric. For $\Omega \neq 0$, the Hamiltonian term induces phase rotation, causing $\rho_{LR}(t)$ to acquire an imaginary component and $m_y \neq 0$, thereby leaving the real half-disk. In symmetric bistable systems (e.g., Duffing potential with $V(-x) = V(x)$, no bias terms), physical symmetry implies $\Delta E = 0$ and hence $\Omega = 0$.

2.7 Two-rate GKSL generator

Having embedded coarse-grained statistics into a density-matrix representation, we now construct a dynamical model for inter-well switching. The model acts on the two-state Hilbert space and governs the evolution of $\rho_{\text{mod}}(t)$, which we fit to the diagonal marginals (populations) extracted from ρ_{emb} .

2.7.1 Why GKSL?

A purely Hamiltonian (unitary) evolution cannot change the populations of a diagonal state when the Hamiltonian is diagonal in the $\{|L\rangle, |R\rangle\}$ basis. Since inter-well switching *is* a population-transfer phenomenon, an effective reduced model must include dissipative (jump) terms. Appendix C gives a formal proof and also explains why common non-Hermitian “dissipative Hamiltonian” tricks lead to nonlinear (non-CPTP) dynamics.

2.7.2 GKSL form and model specification

Definition 2.16 (GKSL master equation). A Markovian, trace-preserving, completely positive master equation on density matrices takes the GKSL form

$$\frac{d\rho}{dt} = -\frac{i}{\hbar}[H, \rho] + \sum_k \left(L_k \rho L_k^\dagger - \frac{1}{2} \{L_k^\dagger L_k, \rho\} \right), \quad (20)$$

where $H = H^\dagger$ and $\{A, B\} = AB + BA$.

Definition 2.17 (Two-state Lindblad model). We use

$$H = -\frac{\Delta E}{2} \sigma_z, \quad (21)$$

$$L_+ = \sqrt{k_{LR}} \sigma_+, \quad (22)$$

$$L_- = \sqrt{k_{RL}} \sigma_-, \quad (23)$$

$$L_d = \sqrt{\kappa} \sigma_z \quad (\text{optional pure dephasing}), \quad (24)$$

with rates $k_{LR}, k_{RL} \geq 0$, dephasing rate $\kappa \geq 0$, and $\Omega = \Delta E/\hbar$.

Remark 2.18 (Interpretation). L_+ and L_- implement population transfers $L \rightarrow R$ and $R \rightarrow L$ at rates k_{LR} and k_{RL} . The L_d term damps off-diagonal elements without changing populations. The GKSL model acts on the reduced two-state space; off-diagonal terms ρ_{LR} in this model represent initial-state uncertainty or mixed preparations, not the coarse-graining overlap $c(\varepsilon)$ defined in Section 2.3. Because symbol observations contain no boundary-proximity information, ρ_{LR} cannot be measured from symbol data and decays to zero at steady state (Section 3.2). The overlap parameter $c(\varepsilon)$ is instead a *coarse-graining diagnostic* that quantifies partition fuzziness for a given ε (Figure 6). Throughout, we use $\rho_{\text{emb}}(t; \varepsilon)$ to denote the embedded state from phase-space data (whose off-diagonal contains $c(\varepsilon)$), see §2.5) and $\rho_{\text{mod}}(t)$ to denote the state governed by this GKSL equation. The model predicts the diagonal part: $[\rho_{\text{mod}}]_{LL} \approx p_L(t) = [\rho_{\text{emb}}]_{LL}$.

Remark 2.19 (Default: symmetric case with $\Omega = 0$). For symmetric bistable potentials (e.g., Duffing with no bias or asymmetry terms), physical symmetry $V(-x) = V(x)$ implies $\Delta E = 0$, yielding $\Omega = 0$. In this case, the half-disk representation remains closed and $m_y = 0$ throughout evolution. Nonzero Ω corresponds to biased or asymmetric potentials and induces phase rotation that mixes real and imaginary components of ρ_{LR} .

2.8 Classical limit on diagonal states

Proposition 2.20 (Reduction to the classical two-state master equation). *If $\rho_{\text{mod}}(t)$ is diagonal in the $\{|L\rangle, |R\rangle\}$ basis, i.e. $\rho_{\text{mod}} = \text{diag}(p_L, 1 - p_L)$, then the GKSL model of Definition 2.17 yields*

$$\frac{dp_L}{dt} = -k_{LR}p_L + k_{RL}(1 - p_L), \quad (25)$$

which is the standard continuous-time two-state (telegraph) master equation with time-homogeneous rates.

Proof. With $\rho_{LR} = 0$, the Hamiltonian commutator vanishes and the dephasing dissipator vanishes on diagonal entries. The jump dissipators generated by L_{\pm} produce the gain/loss terms shown in (25); see Theorem 3.1 below or Appendix A. \square

3 Results: Analytical characterization

Having specified the GKSL model, we now derive explicit evolution equations, closed-form solutions, discrete-time formulations, and an equivalence to Kraus operators. These analytical results provide the mathematical foundation for model fitting and diagnostic testing.

3.1 Evolution equations and Bloch dynamics

For the model state $\rho_{\text{mod}}(t)$, write

$$\rho_{\text{mod}} = \begin{pmatrix} \rho_{LL} & \rho_{LR} \\ \rho_{RL} & \rho_{RR} \end{pmatrix}, \quad \rho_{RL} = \rho_{LR}^*, \quad \rho_{LL} + \rho_{RR} = 1.$$

Theorem 3.1 (Explicit evolution equations). *For the model in Definition 2.17,*

$$\frac{d\rho_{LL}}{dt} = -k_{LR}\rho_{LL} + k_{RL}\rho_{RR}, \quad (26)$$

$$\frac{d\rho_{RR}}{dt} = +k_{LR}\rho_{LL} - k_{RL}\rho_{RR}, \quad (27)$$

$$\frac{d\rho_{LR}}{dt} = \left(i\Omega - \frac{\Gamma}{2} - 2\kappa \right) \rho_{LR}, \quad (28)$$

where $\Gamma = k_{LR} + k_{RL}$.

Remark 3.2. A detailed step-by-step derivation is provided in Appendix A. The result is a linear ODE system: the populations follow a closed two-state rate equation and the off-diagonal term undergoes damped rotation with decay rate $\Gamma/2 + 2\kappa$.

3.1.1 Bloch-vector form

Using $\rho_{\text{mod}} = \frac{1}{2}(\mathbb{I} + \mathbf{m} \cdot \boldsymbol{\sigma})$ with $\mathbf{m} = (m_x, m_y, m_z)$, one obtains

Corollary 3.3 (Bloch-vector evolution). *The Bloch components satisfy*

$$\dot{m}_x = \Omega m_y - \left(\frac{\Gamma}{2} + 2\kappa \right) m_x, \quad (29)$$

$$\dot{m}_y = -\Omega m_x - \left(\frac{\Gamma}{2} + 2\kappa \right) m_y, \quad (30)$$

$$\dot{m}_z = -\Gamma(m_z - m_z^*), \quad m_z^* = \frac{k_{RL} - k_{LR}}{\Gamma}. \quad (31)$$

When $\Omega = 0$ (symmetric case), the evolution remains in the (m_x, m_z) plane with $m_y = 0$, preserving the half-disk embedding from Section 2.3.

3.2 Closed-form solutions and steady state

3.2.1 Steady state

Theorem 3.4 (Steady state of the GKSL model). *Assume $\Gamma = k_{LR} + k_{RL} > 0$. Then the unique stationary state of ρ_{mod} under the GKSL dynamics (20) is diagonal,*

$$\rho_{\text{mod}}^* = \begin{pmatrix} p_L^* & 0 \\ 0 & p_R^* \end{pmatrix}, \quad p_L^* = \frac{k_{RL}}{\Gamma}, \quad p_R^* = \frac{k_{LR}}{\Gamma}. \quad (32)$$

This is consistent with $[\rho_{\text{emb}}]_{LR} = c(\varepsilon) > 0$ for soft partitions, because $c(\varepsilon)$ characterizes the embedding geometry, not a prediction of the symbol-based model.

3.3 Population relaxation

Theorem 3.5 (Population solution for diagonal initial states). *For $\rho_{\text{mod}}(0) = \text{diag}(p_0, 1 - p_0)$,*

$$p_L(t) = p_L^* + (p_0 - p_L^*)e^{-\Gamma t}, \quad (33)$$

and $\rho_{\text{mod}}(t)$ remains diagonal.

The characteristic relaxation time is $\tau_{\text{rel}} = 1/\Gamma$.

3.4 Off-diagonal decay

Theorem 3.6 (Off-diagonal evolution). *For general initial $\rho_{LR}(0)$,*

$$\rho_{LR}(t) = \rho_{LR}(0) \exp \left[\left(i\Omega - \frac{\Gamma}{2} - 2\kappa \right) t \right]. \quad (34)$$

This defines an effective decay time $\tau_{\text{off}} = 1/(\Gamma/2 + 2\kappa)$ for off-diagonal components. The off-diagonal decay describes how initial preparation uncertainty or mixed states evolve under the reduced GKSL dynamics. This is *distinct* from the coarse-graining overlap $c(\varepsilon)$, which characterizes the partition geometry at a given resolution ε (Section 2.3). At steady state, $\rho_{LR}^* = 0$ because symbol data provide no boundary information; the nonzero $c(\varepsilon) > 0$ for soft partitions reflects the embedding choice, not a dynamical prediction.

3.5 Discrete-time Poincaré map and transition matrix

When observations are made once per forcing period T , one can work with a discrete-time transition matrix.

Theorem 3.7 (Discrete-time transition probabilities). *Sampling at interval T , the populations satisfy*

$$p_L^{(n+1)} = p_L^* + (p_L^{(n)} - p_L^*)e^{-\Gamma T}. \quad (35)$$

Equivalently,

$$\begin{pmatrix} p_L \\ p_R \end{pmatrix}_{n+1} = \begin{pmatrix} 1 - P_{LR} & P_{RL} \\ P_{LR} & 1 - P_{RL} \end{pmatrix} \begin{pmatrix} p_L \\ p_R \end{pmatrix}_n, \quad (36)$$

with

$$P_{LR} = p_R^*(1 - e^{-\Gamma T}), \quad P_{RL} = p_L^*(1 - e^{-\Gamma T}). \quad (37)$$

3.6 Rate estimation from symbol data

Given a long symbol sequence $\{S_n\}$, define empirical one-step transition probabilities

$$\hat{P}_{LR} = \frac{\#(L \rightarrow R)}{\#(\text{steps starting in } L)}, \quad \hat{P}_{RL} = \frac{\#(R \rightarrow L)}{\#(\text{steps starting in } R)}.$$

Under the time-homogeneous two-state Markov hypothesis at sampling interval T , one may invert (37):

$$\hat{\Gamma} = -\frac{1}{T} \ln(1 - \hat{P}_{LR} - \hat{P}_{RL}), \quad (38)$$

$$\hat{k}_{LR} = \frac{\hat{P}_{LR}}{\hat{P}_{LR} + \hat{P}_{RL}} \hat{\Gamma}, \quad \hat{k}_{RL} = \frac{\hat{P}_{RL}}{\hat{P}_{LR} + \hat{P}_{RL}} \hat{\Gamma}. \quad (39)$$

Section 4 emphasizes that these formulas should be used only after Markov diagnostics support the assumed closure at the chosen sampling scale.

4 Results: Diagnostic framework

The analytical results derived in Section 3 rely on the assumption that the coarse-grained symbol sequence $\{S_n\}$ satisfies a time-homogeneous first-order Markov property. This section develops a complete diagnostic framework with four complementary tests that can falsify this assumption, provides practical guidance for sparse data and threshold selection, and outlines systematic extensions when higher-order memory is detected.

4.1 Hypotheses and test structure

Definition 4.1 (First-order Markov property). $\{S_n\}$ is first-order Markov if for all $i, j \in \{L, R\}$,

$$\Pr(S_{n+1} = j \mid S_n = i, S_{n-1}, \dots) = \Pr(S_{n+1} = j \mid S_n = i) =: P_{ij}.$$

Definition 4.2 (Time homogeneity). The chain is time homogeneous if P_{ij} does not depend on n after transients.

4.2 Order test: does conditioning on S_{n-1} change transitions?

Define counts

$$N_{kij} = \#\{n : S_{n-1} = k, S_n = i, S_{n+1} = j\}, \quad N_{ki} = \sum_j N_{kij}, \quad N_{ij} = \sum_k N_{kij}.$$

Define empirical probabilities

$$\hat{P}_{ij} = \frac{N_{ij}}{\sum_{j'} N_{ij'}}, \quad \hat{P}_{ij|k} = \frac{N_{kij}}{N_{ki}}.$$

A standard likelihood-ratio statistic for first-order vs second-order structure is

$$G = 2 \sum_{k,i,j} N_{kij} \ln \left(\frac{\hat{P}_{ij|k}}{\hat{P}_{ij}} \right), \quad (40)$$

which is asymptotically χ^2 distributed under the null (large-sample regime). If G is large relative to the appropriate degrees of freedom, first-order Markovity is rejected. For the G-test comparing first-order vs. second-order Markov models, the degrees of freedom are

$$\text{df} = d(d-1)^2, \quad (41)$$

where d is the number of states. For the binary case ($d = 2$), $\text{df} = 2$. At significance level $\alpha = 0.05$, the critical value is $\chi_{2,0.05}^2 \approx 5.99$. The empirical p -value is computed as $p = \Pr(\chi_2^2 \geq G)$. The null hypothesis of first-order Markovity is rejected if $p < \alpha$.

Remark 4.3 (Implementation and sparse-count handling). In computing G , terms with $N_{kij} = 0$ are omitted (the limit $0 \log 0 = 0$). When some N_{kij} are small (say < 5), the asymptotic χ^2 approximation may be unreliable. Three practical remedies are recommended:

- (a) **Pseudocount smoothing:** Add a small Laplace pseudocount $\delta \in [0.5, 1]$ to all counts: $N_{kij} \rightarrow N_{kij} + \delta$. Report the p -value for $\delta = 0$ (no smoothing) and $\delta = 0.5$ to assess sensitivity.
- (b) **Permutation test:** If many cells have $N_{kij} < 5$, replace the χ^2 reference distribution with a permutation test: shuffle the symbol sequence $\{S_n\}$ randomly (preserving marginals), recompute G^{perm} , and repeat 1000–10000 times to build an empirical null distribution. Reject if the observed G exceeds the 95th percentile of G^{perm} .
- (c) **Bootstrap confidence intervals:** Use block bootstrap (preserving temporal dependence) to obtain confidence intervals on G and assess whether the observed value is significantly different from the null expectation.

For typical high-resolution Duffing simulations with $N \geq 10^4$ samples, the asymptotic χ^2 approximation is generally adequate, but for short sequences ($N < 500$) or highly imbalanced partitions, permutation or bootstrap approaches are more robust.

4.3 Chapman–Kolmogorov consistency

For a time-homogeneous Markov chain with one-step matrix \mathbf{P} , the Chapman–Kolmogorov equation requires $\mathbf{P}^{(2)} = \mathbf{P}^2$ for the two-step transition matrix. To test this hypothesis, empirically estimate $\hat{\mathbf{P}}$ (one-step) and $\hat{\mathbf{P}}^{(2)}$ (two-step) from the symbol sequence and compute the Frobenius-norm discrepancy:

$$\Delta_{\text{CK}} = \left\| \hat{\mathbf{P}}^{(2)} - \hat{\mathbf{P}}^2 \right\|_F.$$

Bootstrap hypothesis test. To assess whether observed discrepancy is statistically significant, we perform a bootstrap test under H_0 : the process is first-order Markov. The procedure is summarized in Table 1.

Table 1: Bootstrap hypothesis test for Chapman–Kolmogorov consistency

Step	Description
1. Generate data	Generate B (e.g., $B = 1000$) synthetic sequences of length N from a first-order Markov chain with transition matrix $\hat{\mathbf{P}}$.
2. Bootstrap loop	For each bootstrap replicate $b = 1, \dots, B$: (a) Estimate $\hat{\mathbf{P}}^{*,b}$ (one-step) and $\hat{\mathbf{P}}^{(2),*,b}$ (two-step) from the synthetic sequence. (b) Compute $\Delta_{\text{CK}}^{*,b} = \left\ \hat{\mathbf{P}}^{(2),*,b} - (\hat{\mathbf{P}}^{*,b})^2 \right\ _F$.
3. Compute p -value	Compute the empirical p -value: $p_{\text{CK}} = \frac{1 + \#\{b: \Delta_{\text{CK}}^{*,b} \geq \Delta_{\text{CK}}^{\text{obs}}\}}{B+1}$.
4. Confidence interval	Construct a 95% confidence interval using bootstrap quantiles: $\text{CI}_{95\%} = [\Delta_{\text{CK}}^{*,(0.025B)}, \Delta_{\text{CK}}^{*,(0.975B)}]$.
5. Decision	Reject the first-order Markov hypothesis if $p_{\text{CK}} < 0.05$.

Large values of Δ_{CK} relative to the bootstrap distribution, or equivalently small p_{CK} , indicate that a single time-homogeneous Markov matrix is insufficient at the sampling scale, suggesting higher-order memory effects or time-inhomogeneity. When rejection occurs, see Section 4.6 for standard extensions (higher-order Markov, hidden Markov, semi-Markov). However, Chapman–Kolmogorov consistency at a given order is necessary but not sufficient for embedding the empirical transition matrix into a continuous-time GKSL semigroup; the latter requires additional spectral conditions on the transition matrix. When continuous-time embedding is uncertain or fails, the discrete-time Kraus representation remains a valid, model-free approach to ensure complete positivity and trace preservation.

4.4 Run-length (dwell-time) statistics

If $\{S_n\}$ is Markov with one-step probability P_{LR} , then the run length R_L of consecutive L 's is geometric:

$$\Pr(R_L = r) = (1 - P_{LR})^{r-1} P_{LR}, \quad r \geq 1,$$

and similarly for R -runs. Comparing empirical run-length histograms to these geometric laws is a direct test of memorylessness. Figure 4 presents run-length distributions for both wells.

Remark 4.4 (Well-dependent dwell-time behavior). Experimental observations in chaotic bistable systems often reveal asymmetric run-length statistics. For instance, the left well may exhibit predominantly short runs (1–3 periods) while the right well displays a broader distribution (1–15 periods). Such well-dependent behavior can arise from asymmetric potential structure or differences in local escape mechanisms, and typically indicates deviations from a simple geometric law. These deviations point to either higher-order memory or non-geometric (semi-Markov) waiting-time distributions.

4.5 Windowed stationarity test

Split the post-transient sequence into W windows (typically $W = 5$ to 10) of equal length and compute the transition probabilities $\hat{P}_{LR}^{(w)}, \hat{P}_{RL}^{(w)}$ for each window $w = 1, \dots, W$. Systematic drift beyond sampling variability suggests nonstationarity or time-dependent effective rates.

Quantitative threshold criteria. Three complementary approaches quantify whether observed window-to-window variation exceeds chance:

- Confidence-interval overlap:** Compute 95% Wald confidence intervals for each $\hat{P}_{LR}^{(w)}$ (using $\text{SE} = \sqrt{\hat{P}_{LR}(1 - \hat{P}_{LR})/N_w}$, where N_w is the number of L states in window w). Reject stationarity if intervals from different windows fail to overlap.
- Heterogeneity test:** Perform a χ^2 test for homogeneity across windows: compute $\chi^2 = \sum_{w=1}^W \frac{(\hat{P}_{LR}^{(w)} - \bar{P}_{LR})^2}{\text{Var}[\hat{P}_{LR}^{(w)}]}$, where \bar{P}_{LR} is the pooled estimate. Under stationarity, $\chi^2 \sim \chi_{W-1}^2$.

- (c) **Change-point detection:** Apply a standard change-point algorithm (e.g., binary segmentation or PELT [26]) to the time series $\{\hat{P}_{LR}^{(w)}\}_{w=1}^W$. Reject stationarity if a change point is detected at significance level $\alpha = 0.05$.

For typical Duffing simulations with steady forcing, confidence-interval overlap (approach a) is simplest and most transparent. If nonstationarity is detected, a time-dependent generator $k_{LR}(t)$, $k_{RL}(t)$ or a richer coarse-graining (e.g., phase-resolved partitions) is required.

4.6 If tests fail: controlled extensions

If the diagnostics reject the first-order time-homogeneous model, standard extensions are available. First, one may adopt **higher-order Markov** models by augmenting the state space to words (e.g. $\{LL, LR, RL, RR\}$) so that the process becomes first-order in the enlarged space; for a second-order Markov model, the GKSL framework can be extended to a 4×4 density matrix acting on the enlarged Hilbert space $\mathcal{H}_{2\text{-step}} = \text{span}\{|LL\rangle, |LR\rangle, |RL\rangle, |RR\rangle\}$, with jump operators encoding transitions among these four states. Second, **hidden Markov** models may include a latent variable correlated with switching (e.g. drive phase or energy bin). Third, **semi-Markov** approaches explicitly model non-geometric run lengths (non-exponential waiting times). Fourth, one may allow **time-dependent rates** by fitting piecewise-constant or periodically modulated rate functions. These modifications preserve the core “two-lobe coarse-graining” idea while making memory and nonstationarity explicit.

Remark 4.5 (Experimental evidence of second-order effects). High-resolution experimental data from deterministic Duffing simulations may reveal statistically significant second-order memory effects. For example, the order test (Section 4) may yield a G-statistic with $p \ll 0.01$, rejecting the first-order null hypothesis. Such findings do *not* invalidate the GKSL framework; they indicate that the coarse-grained process at the chosen sampling scale is better described by a higher-order Markov model or a hidden Markov model. Importantly, the Chapman–Kolmogorov consistency test (Section 4) can still hold, confirming that the Markov property is satisfied at a higher order and that the framework remains applicable with appropriate state-space augmentation.

Remark 4.6 (Caveat: not all discrete-time processes embed into continuous-time generators). While augmenting the state space to words allows construction of first-order Markov models in the enlarged space, not every such discrete-time transition matrix admits a representation as $\mathbf{P} = e^{\mathbf{Q}T}$ for a time-independent GKSL generator \mathbf{Q} . This is the classical *Markov embedding problem*: empirical transition matrices may violate necessary spectral conditions for continuous-time embedding.

Practical embedding diagnostics. For a two-state system, the embedding problem is usually tractable: a stochastic matrix \mathbf{P} can be embedded in continuous time if and only if its eigenvalues are positive and the off-diagonal rates derived from the matrix logarithm are nonnegative. For higher-dimensional systems (e.g., four-state second-order extensions), the following checks are recommended:

- (a) **Eigenvalue positivity:** Verify that all eigenvalues of $\hat{\mathbf{P}}$ are strictly positive. Negative or complex eigenvalues with negative real parts preclude continuous-time embedding.
- (b) **Matrix logarithm and rate extraction:** Compute $\mathbf{Q} = \frac{1}{T} \log \hat{\mathbf{P}}$ (using matrix logarithm). Check that the off-diagonal entries of \mathbf{Q} (interpreted as jump rates) are nonnegative and that diagonal entries satisfy $Q_{ii} = -\sum_{j \neq i} Q_{ij}$. If rates are negative or the semigroup constraint fails, continuous embedding does not exist.
- (c) **Semigroup consistency:** Verify Chapman–Kolmogorov consistency at multiple time steps: check that $\hat{\mathbf{P}}^{(kT)} \approx (\hat{\mathbf{P}}^{(T)})^k$ for $k = 2, 3, \dots$. Large deviations suggest time-inhomogeneity or non-semigroup structure, ruling out a time-independent GKSL generator.

When these diagnostics fail, we recommend working directly with the discrete-time CPTP map (Kraus representation) as the fundamental object, rather than attempting to infer a continuous-time GKSL generator. Continuous-time GKSL generators should only be inferred when the data structure and Chapman–Kolmogorov tests strongly support time-homogeneous semigroup closure. For two-state systems with typical Duffing parameters, continuous embedding usually succeeds; for higher-order extensions or systems with complex memory structure, discrete-time Kraus operators are often more appropriate.

4.7 Kraus representation and equivalence to generalized amplitude damping

The continuous-time GKSL evolution $\frac{d\rho}{dt} = \mathcal{L}[\rho]$ can be integrated to yield a discrete-time completely positive trace-preserving (CPTP) map $\rho(t+T) = \Phi_T[\rho(t)]$. For finite-time propagation, this map admits a Kraus (operator-sum)

representation, which we now derive explicitly and prove equivalence to the well-known generalized amplitude damping (GAD) channel composed with dephasing and phase rotation.

Notation. In this section we write ρ for the model state ρ_{mod} to simplify notation in the Kraus-operator expressions. Beyond the differential equation form, it is often useful to express the evolution as an operator-sum (Kraus) representation

$$\rho(t) = \Lambda_t(\rho(0)) = \sum_{\ell} K_{\ell}(t)\rho(0)K_{\ell}(t)^{\dagger}, \quad \sum_{\ell} K_{\ell}(t)^{\dagger}K_{\ell}(t) = \mathbb{I},$$

which makes complete positivity and trace preservation explicit.

For the two-rate model in Definition 2.17, one can construct a Kraus family by composing: (i) a generalized amplitude-damping channel encoding population relaxation toward ρ^* , (ii) a phase-damping channel encoding dephasing with rate κ , and (iii) a unitary phase rotation generated by H .

4.8 Kraus operators

Define

$$\Gamma = k_{LR} + k_{RL}, \quad \lambda(t) = 1 - e^{-\Gamma t}, \quad \eta(t) = e^{-2\kappa t}, \quad p_R^* = \frac{k_{LR}}{\Gamma}, \quad p_L^* = \frac{k_{RL}}{\Gamma}.$$

Let

$$U(t) = e^{-iHt/\hbar} = \exp\left(+i\frac{\Omega t}{2}\sigma_z\right) = \begin{pmatrix} e^{+i\Omega t/2} & 0 \\ 0 & e^{-i\Omega t/2} \end{pmatrix}.$$

Introduce generalized-amplitude-damping Kraus operators

$$E_0(t) = \sqrt{p_L^*} \begin{pmatrix} 1 & 0 \\ 0 & \sqrt{1-\lambda(t)} \end{pmatrix}, \quad E_1(t) = \sqrt{p_L^*} \begin{pmatrix} 0 & \sqrt{\lambda(t)} \\ 0 & 0 \end{pmatrix}, \quad (42)$$

$$E_2(t) = \sqrt{p_R^*} \begin{pmatrix} \sqrt{1-\lambda(t)} & 0 \\ 0 & 1 \end{pmatrix}, \quad E_3(t) = \sqrt{p_R^*} \begin{pmatrix} 0 & 0 \\ \sqrt{\lambda(t)} & 0 \end{pmatrix}, \quad (43)$$

and phase-damping Kraus operators

$$F_0(t) = \sqrt{\frac{1+\eta(t)}{2}} \mathbb{I}, \quad F_1(t) = \sqrt{\frac{1-\eta(t)}{2}} \sigma_z. \quad (44)$$

Define the composite family

$$M_{aj}(t) = U(t) F_a(t) E_j(t), \quad a \in \{0, 1\}, \quad j \in \{0, 1, 2, 3\}. \quad (45)$$

Lemma 4.7 (Completeness). *The operators $M_{aj}(t)$ satisfy $\sum_{a=0}^1 \sum_{j=0}^3 M_{aj}(t)^{\dagger} M_{aj}(t) = \mathbb{I}$.*

Remark 4.8. Lemma 4.7 implies that $\Lambda_t(\rho) = \sum_{a,j} M_{aj}(t)\rho M_{aj}(t)^{\dagger}$ is CPTP. A direct calculation also shows that this map reproduces the closed-form GKSL solutions for populations and off-diagonals; see Theorem 4.9 and Appendix B.

Theorem 4.9 (Equivalence to the GKSL solution). *Let $\Lambda_t(\rho) = \sum_{a,j} M_{aj}(t)\rho M_{aj}(t)^{\dagger}$ with (45). Then for any initial state $\rho(0)$,*

$$\rho_{LL}(t) = p_L^* + (\rho_{LL}(0) - p_L^*)e^{-\Gamma t}, \quad (46)$$

$$\rho_{LR}(t) = \rho_{LR}(0) \exp\left[\left(i\Omega - \frac{\Gamma}{2} - 2\kappa\right)t\right]. \quad (47)$$

Hence Λ_t coincides with the GKSL evolution generated by Definition 2.17.

Remark 4.10 (Interpretational note). The Kraus representation is a statement about the *reduced two-state model*. It does not imply that the underlying Duffing dynamics is quantum; rather, it provides a mathematically consistent CPTP parametrization for the coarse-grained statistics.

5 Numerical methods

This section outlines computational validation procedures for applying the framework to Duffing or other bistable systems. We provide a concise protocol for integration, symbol generation, diagnostic testing, and rate estimation to facilitate reproducible numerical studies.

5.1 Simulation and sampling protocol

Integrate the driven Duffing system (1) using a stable ODE solver (e.g., 4th-order Runge–Kutta or adaptive Dormand–Prince) with time step $\Delta t \ll T$ where $T = 2\pi/\omega$ is the forcing period. For stochastic extensions (3) with noise intensity $D > 0$, use Euler–Maruyama or higher-order SDE schemes. Discard initial transients (typically 50–100 periods) and collect N Poincaré samples at times $t_n = nT$ over 200–500 periods to ensure adequate statistics for diagnostic tests. Verify numerical convergence by halving Δt and checking that transition probabilities change by less than 1%.

5.2 Symbol generation and soft memberships

Construct hard symbols $\{S_n\}$ using Definition 2.2 (sign-based partition) or a refined boundary function $g(z)$ based on approximate separatrix geometry. For soft-partition analysis, compute membership weights $w_L(z_n), w_R(z_n)$ via Definition 2.4 for a grid of fuzziness parameters $\varepsilon \in [10^{-2}, 10^1]$. Estimate the embedded state ρ_{emb} and overlap parameter $c(\varepsilon)$ via Proposition 2.8, and plot $c(\varepsilon)$ vs. ε to verify the hard-partition limit $c(\varepsilon) \rightarrow 0$ as $\varepsilon \rightarrow 0^+$ (Figure 6).

5.3 Diagnostic testing

Apply the four tests developed in Section 4 to the symbol sequence $\{S_n\}$:

- (a) **Order test:** Compute G-statistic via (40) and report p -value; reject first-order Markov if $p < 0.05$.
- (b) **Chapman–Kolmogorov:** Estimate $\hat{\mathbf{P}}$ and $\hat{\mathbf{P}}^{(2)}$, compute discrepancy $\Delta_{\text{CK}} = \|\hat{\mathbf{P}}^{(2)} - \hat{\mathbf{P}}^2\|_F$, and obtain bootstrap confidence intervals using the procedure in Table 1.
- (c) **Run-length distributions:** Plot histograms of run lengths for L and R states, overlay geometric fits, and assess goodness-of-fit via χ^2 test.
- (d) **Windowed stationarity:** Divide the steady-state sequence into $W = 5$ to 10 windows, estimate $\hat{P}_{LR}^{(w)}$ for each window, and test for heterogeneity using confidence-interval overlap or χ^2 test.

If diagnostics reject first-order Markov closure, apply the state-space augmentation protocols outlined in Section 4.6.

5.4 Rate estimation and model validation

If Markov diagnostics pass, estimate switching rates via the inversion formulas (38) and (39). Compare model-predicted populations $p_L(t)$ (from solving (26)–(27) with estimated rates) against empirical populations from windowed time averages. Quantify agreement using mean absolute error or Kullback–Leibler divergence. Report estimated rates $\hat{k}_{LR}, \hat{k}_{RL}$, steady-state populations p_L^* , and relaxation time $\tau = 1/\hat{\Gamma}$ with confidence intervals obtained via block bootstrap resampling (Table 2).

6 Discussion

Soft memberships. Fix $g(z)$ and a fuzziness parameter ε , then compute $w_L(z(t_n)), w_R(z(t_n))$ by (10). Estimate

$$\hat{c}(\varepsilon) = \frac{1}{N} \sum_{n=1}^N \sqrt{w_L(z(t_n))w_R(z(t_n))}. \quad (48)$$

Repeat for a grid of ε values to verify $\hat{c}(\varepsilon) \rightarrow 0$ as $\varepsilon \rightarrow 0^+$.

6.1 Estimating transition probabilities and continuous-time rates

Compute the transition counts

$$N_{LL}, N_{LR}, N_{RL}, N_{RR},$$

and the empirical one-step probabilities $\hat{P}_{LR}, \hat{P}_{RL}$. Then reconstruct $\hat{\Gamma}, \hat{k}_{LR}, \hat{k}_{RL}$ using (38)–(39). Report confidence intervals, e.g. by binomial standard errors or block bootstrap (Table 2; the latter is preferred if serial correlations are strong).

6.2 Block bootstrap for confidence intervals on transition probabilities

When serial correlation is strong in the symbol sequence (e.g., due to quasi-periodic dynamics or memory effects), standard binomial confidence intervals for estimated transition probabilities \hat{P}_{LR} and \hat{P}_{RL} are too narrow. We employ the block bootstrap [27, 28] to obtain robust confidence intervals.

Block length selection. The optimal block length ℓ balances bias (too short blocks lose dependency structure) and variance (too long blocks reduce effective sample size). A practical choice is

$$\ell \approx 2\tau_{\text{int}}, \quad (49)$$

where τ_{int} is the integrated autocorrelation time of the indicator process $I[S_n = L]$, estimated via

$$\hat{\tau}_{\text{int}} = 1 + 2 \sum_{k=1}^{K_{\text{max}}} \hat{\rho}(k),$$

with $\hat{\rho}(k)$ the sample autocorrelation function truncated at a suitable lag K_{max} (e.g., first zero crossing or $K_{\text{max}} = \lfloor N^{1/3} \rfloor$). Alternatively, overlapping (moving) blocks can increase the number of distinct resampled blocks; the stationary bootstrap [27] provides an automatic adaptive procedure.

Block bootstrap algorithm. The block bootstrap procedure for computing confidence intervals on transition probabilities and rate parameters is detailed in Table 2.

Table 2: Block bootstrap algorithm for confidence intervals on transition probabilities

Step	Description
1. Block division	Divide the post-transient sequence $\{S_1, \dots, S_N\}$ into $m = \lfloor N/\ell \rfloor$ contiguous, non-overlapping blocks of length ℓ .
2. Bootstrap loop	For $b = 1, \dots, B$ bootstrap replicates (e.g., $B = 1000$): (a) Randomly draw m blocks with replacement from the m available blocks. (b) Concatenate to form a bootstrap sequence $\{S_1^*, \dots, S_N^*\}$. (c) Compute bootstrap estimates: $\hat{P}_{LR}^{*,b}$, $\hat{P}_{RL}^{*,b}$, and (if desired) $\hat{k}_{LR}^{*,b}$, $\hat{k}_{RL}^{*,b}$ using Eqs. (38)–(39).
3. Confidence intervals	Construct 95% confidence intervals using the percentile method: $\text{CI}_{95\%} = [\hat{\theta}^{*,(0.025B)}, \hat{\theta}^{*,(0.975B)}]$, where $\hat{\theta}^{*,(q)}$ denotes the q -th empirical quantile of the bootstrap replicates $\{\hat{\theta}^{*,1}, \dots, \hat{\theta}^{*,B}\}$. (Eq. 50)
4. Standard error	Compute block-bootstrap standard error: $\widehat{\text{SE}}_{\text{block}} = \sqrt{\frac{1}{B} \sum_{b=1}^B (\hat{\theta}^{*,b} - \bar{\theta}^*)^2}$, where $\bar{\theta}^* = \frac{1}{B} \sum_{b=1}^B \hat{\theta}^{*,b}$. (Eq. 51)

$$\text{CI}_{95\%} = [\hat{\theta}^{*,(0.025B)}, \hat{\theta}^{*,(0.975B)}] \quad (50)$$

$$\widehat{\text{SE}}_{\text{block}} = \sqrt{\frac{1}{B} \sum_{b=1}^B (\hat{\theta}^{*,b} - \bar{\theta}^*)^2}, \quad \bar{\theta}^* = \frac{1}{B} \sum_{b=1}^B \hat{\theta}^{*,b} \quad (51)$$

Reporting. When presenting estimated rates, report the block-bootstrap point estimate and 95% confidence interval. For example:

$$\hat{k}_{LR} = 0.42 \text{ (95\% CI: [0.38, 0.46])}.$$

This acknowledges serial correlation and provides a more honest quantification of uncertainty than standard errors assuming independence.

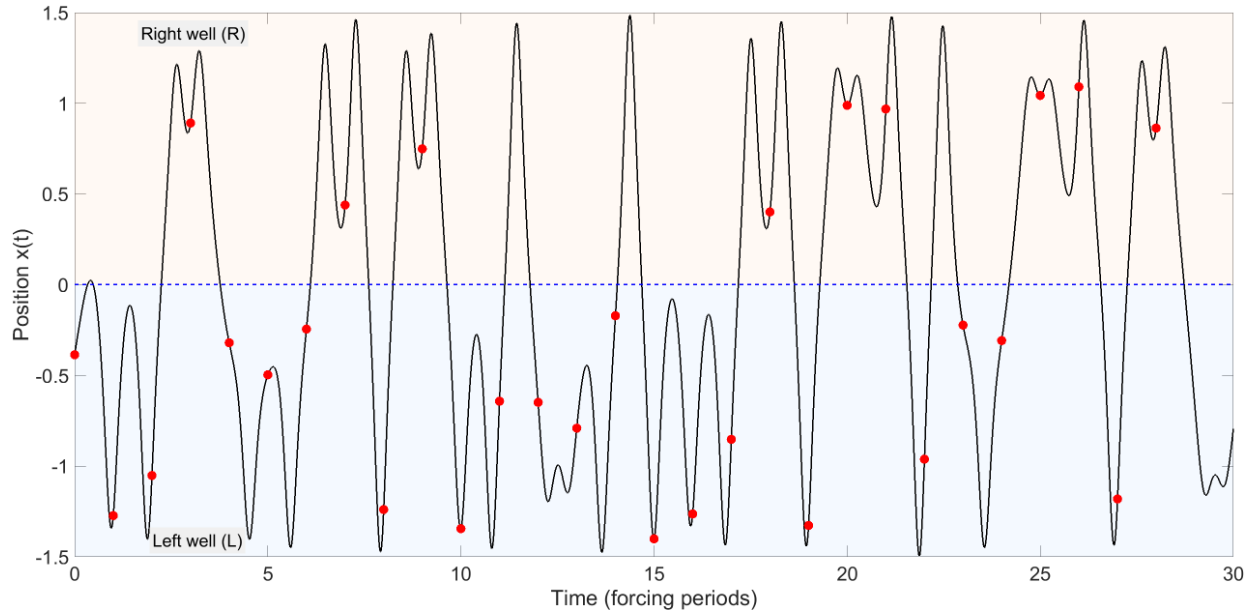


Figure 1: Representative time series $x(t)$ in a chaotic bistable regime, with the two wells indicated (e.g. $x < 0$ and $x > 0$ regions) and stroboscopic sampling points marked. This figure justifies that the chosen parameter set exhibits inter-well hopping on the observation horizon.

Table 3: Transition counts and one-step probabilities at sampling interval T . Replace the angle-bracket placeholders $\langle \cdot \rangle$ with empirical values.

	to L	to R
from L	$\langle N_{LL} \rangle$	$\langle N_{LR} \rangle$
from R	$\langle N_{RL} \rangle$	$\langle N_{RR} \rangle$
\hat{P}_{LR}	$\langle \hat{P}_{LR} \rangle$	
\hat{P}_{RL}	$\langle \hat{P}_{RL} \rangle$	

6.3 Model checks (Markov diagnostics)

Apply the diagnostics in Section 4. Specifically, perform the order test via (40), compute the Chapman–Kolmogorov discrepancy Δ_{CK} , compare the run-length histogram against the geometric law, and assess windowed stationarity of $\hat{P}_{LR}, \hat{P}_{RL}$. If diagnostics fail, explicitly switch to an extended model and report the extension (higher-order, hidden Markov, semi-Markov, or time-dependent rates).

6.4 Figure and table templates

The following placeholders are designed to be replaced by your computed outputs.

6.5 Minimal reporting checklist

To make the numerical study reproducible and the statistical claims falsifiable, we recommend reporting six key items. First, provide full Duffing parameters $(\alpha, \beta, \delta, \gamma_0, \omega)$ and solver details (integrator, Δt , convergence checks). Second, specify the sampling scheme (Poincaré period T , window length Δ if used). Third, report total samples N and transient discarded N_{trans} . Fourth, present transition counts and estimated $(\hat{P}_{LR}, \hat{P}_{RL})$, together with reconstructed rates $(\hat{k}_{LR}, \hat{k}_{RL})$ with uncertainty. Fifth, document Markov diagnostic outcomes (order test statistic/p-value, CK discrepancy, run-length fits, stationarity results). Sixth, if diagnostics fail, report the chosen extension and its fitted parameters.

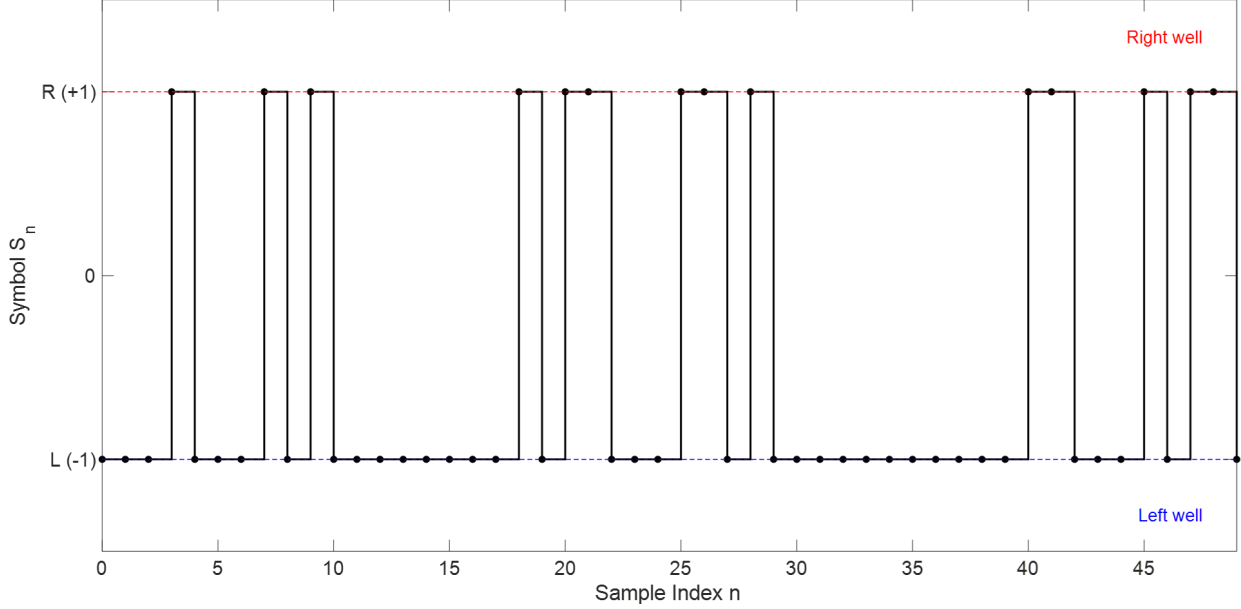


Figure 2: Example segment of the binary symbol sequence $\{S_n\}$ (or equivalently the sign of $x(t_n)$) illustrating dwell times and switching events.

Table 4: Reconstructed continuous-time rates from (38)–(39). Report uncertainty estimates.

Quantity	Estimate
$\hat{\Gamma}$	$\langle \hat{\Gamma} \pm \text{SE} \rangle$
\hat{k}_{LR}	$\langle \hat{k}_{LR} \pm \text{SE} \rangle$
\hat{k}_{RL}	$\langle \hat{k}_{RL} \pm \text{SE} \rangle$

7 Discussion and limitations

7.1 What the framework provides

At the level of diagonal states, the two-rate GKSL model is equivalent to the classical two-state master equation. The value of the Lindblad–Pauli presentation is therefore not in changing the underlying stochastic assumption, but in *organizing* it: the GKSL generator makes CPTP structure explicit, the Kraus form provides a constructive channel representation, and the Bloch parametrization offers a geometric view of the reduced state space.

The soft-partition embedding adds an additional operational parameter $c(t)$ that captures boundary overlap of the coarse-grained distribution. Even though $c(t)$ is not a microscopic quantum coherence, it is a well-defined functional of the chosen coarse-graining and can be estimated from data. This may be useful when comparing different coarse-grainings or quantifying the effect of finite resolution/windowing on inferred switching statistics.

Crucially, $c(\varepsilon)$ is *not* the same as the off-diagonal element ρ_{LR} in the GKSL model. The GKSL dynamics govern populations from symbol observations; off-diagonal terms in this model represent initial-state uncertainty and decay to zero at steady state (Theorem 3.4). In contrast, $c(\varepsilon)$ is computed directly from phase-space data and characterizes the chosen partition resolution. Figure 6 shows $c(\varepsilon)$ as a function of the fuzziness parameter, demonstrating that sharper partitions ($\varepsilon \rightarrow 0$) yield $c \rightarrow 0$ (classical limit), while soft partitions have $c(\varepsilon) > 0$. This diagnostic helps select an appropriate coarse-graining scale by balancing resolution (small ε , $c \approx 0$) against the need to avoid spurious boundary-crossing artifacts in chaotic trajectories.

7.2 Limitations

Model closure. A two-state Markov closure can fail if (i) switching is influenced by slow variables (energy, phase, or intra-well chaotic motion) that retain memory across sampling steps, (ii) the observation interval T is not well separated

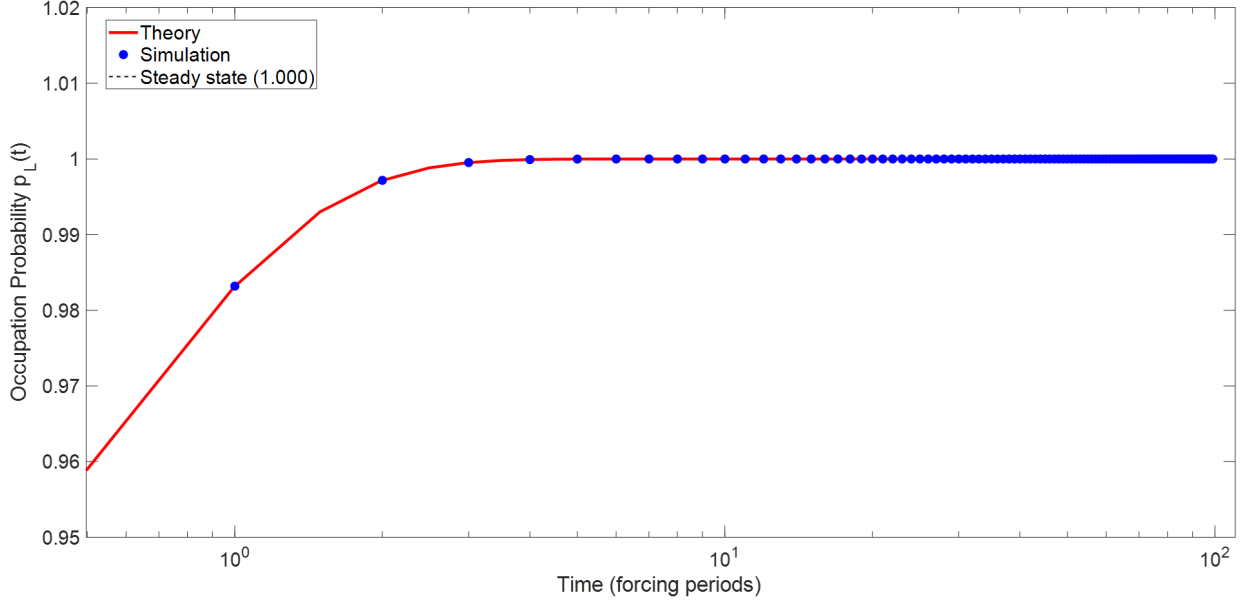


Figure 3: Population relaxation: comparison of the theoretical curve $p_L(t) = p_L^* + (p_0 - p_L^*)e^{-\Gamma t}$ (Theorem 3.5) to an ensemble-averaged estimate of $p_L(t)$ from simulation, started from biased initial conditions.

from relevant correlation times, or (iii) the system exhibits nonstationary regimes. Section 4 provides diagnostics and standard extensions.

Interpretation of off-diagonal terms. The off-diagonal term $c(t)$ is embedding-dependent. If only L/R occupancy is measured, $c(t)$ cannot be inferred uniquely without additional operational definitions (boundary observables). Thus $c(t)$ should be treated as a coarse-graining descriptor rather than as an intrinsic property of the underlying continuous dynamics.

Parameter dependence. The rates k_{LR}, k_{RL} are phenomenological in this framework. Deriving them from first principles for deterministic chaotic switching is nontrivial and generally requires additional dynamical-systems analysis. Our emphasis is on measurable inference and falsifiable reduced modeling.

7.3 Model order and extensions

Experimental validation of the first-order Markov assumption is critical. High-resolution numerical experiments on deterministic Duffing systems can reveal statistically significant second-order memory effects, as evidenced by order tests (e.g., G-test with $p \approx 0.001$). Such findings indicate that the coarse-grained symbol sequence $\{S_n\}$ at the chosen sampling interval retains memory of the previous two states rather than just the immediate predecessor.

Interpretation and framework validity. The presence of second-order memory does *not* undermine the GKSL framework. Rather, it signals that the effective state space should be augmented. For a second-order Markov process, one can construct a 4×4 density matrix on the Hilbert space $\mathcal{H}_{2\text{-step}} = \text{span}\{|LL\rangle, |LR\rangle, |RL\rangle, |RR\rangle\}$, and define jump operators L_{ijkl} that map $(S_{n-1}, S_n) \rightarrow (S_n, S_{n+1})$. This enlarged GKSL model is first-order Markov in the augmented state and can capture the second-order dependencies observed experimentally.

Chapman–Kolmogorov as validation. Crucially, the Chapman–Kolmogorov consistency test can still hold even when first-order order tests fail. This indicates that the process is Markov at a higher order, and that the GKSL formalism remains applicable with an appropriately enlarged state space. The framework’s value lies in its systematic approach to constructing completely positive trace-preserving (CPTP) maps, which remains valid regardless of the order of the Markov model.

Practical recommendations. When experimental diagnostics reject the first-order assumption, several extensions are available. One may augment the state space to pairs or triplets of symbols (Section 4.6). Alternatively, one may

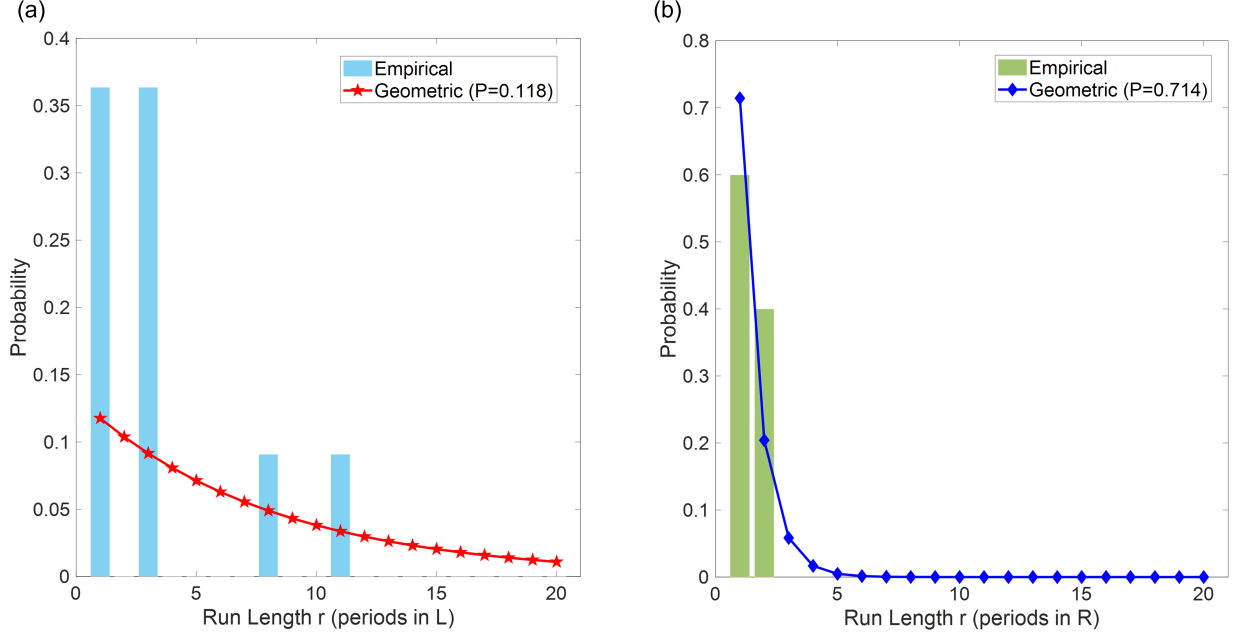


Figure 4: Run-length (dwell-time) distributions testing the memoryless property of first-order Markov chains. (a) Left-well run lengths: empirical histogram (blue bars) compared to geometric distribution $\Pr(R_L = r) = (1 - P_{LR})^{r-1} P_{LR}$ (red curve) with transition probability \hat{P}_{LR} estimated from data. (b) Right-well run lengths: empirical histogram (orange bars) compared to geometric distribution $\Pr(R_R = r) = (1 - P_{RL})^{r-1} P_{RL}$ (blue curve) with transition probability \hat{P}_{RL} estimated from data. Deviations from geometric laws diagnose non-Markov or time-inhomogeneous behavior at the sampling scale. Parameters: $\alpha = 1.0$, $\beta = 1.0$, $\delta = 0.15$, $\gamma_0 = 0.3$, $\omega = 1.0$.

consider hidden Markov models (HMMs) that include latent variables such as drive phase or energy level. For systems with well-dependent dwell-time statistics, semi-Markov models with explicit waiting-time distributions may be more parsimonious.

7.4 Extensions and model diagnostics

Natural next steps include: multi-state coarse-grainings (e.g., adding a boundary state), time-dependent generators, semi-Markov dwell-time models, and systematic comparisons between hard- and soft-partition embeddings. Each extension inherits the CPTP structure and remains amenable to the same diagnostic framework.

Quantum information tools for model diagnostics. Because the coarse-grained evolution satisfies CPTP properties (automatic from GKSL form), standard quantum-information quantities provide objective model-selection and validation metrics. **Purity** $\text{Tr}(\rho_{\text{emb}}^2)$ quantifies the classicality of the effective state: high purity ($\rightarrow 1$) signals clean binary switching, while reduced purity (< 0.9) indicates significant partition overlap or missing state-space degrees of freedom. Plotting purity vs. coarse-graining resolution ε identifies the resolution-vs.-purity trade-off. **Fidelity** $F(\rho_{\text{mod}}, \rho_{\text{emb}}) = \text{Tr} \sqrt{\sqrt{\rho_{\text{emb}}} \rho_{\text{mod}} \sqrt{\rho_{\text{emb}}}}$ measures agreement between GKSL predictions and empirical densities; maximizing fidelity over parameters (k_{LR}, k_{RL}) performs nonparametric rate estimation, and fidelity thresholds (e.g., $F > 0.95$) validate model adequacy on held-out data. **Trace distance** $D_{\text{tr}}(\rho_{\text{hard}}, \rho_{\text{soft}}) = \frac{1}{2} \text{Tr} |\rho_{\text{hard}} - \rho_{\text{soft}}|$ assesses robustness to partition-width choices: small D_{tr} across a range of ε indicates stable inferred rates, whereas large D_{tr} indicates partition sensitivity and suggests the need for higher-resolution coarse-grainings.

Data requirements. These metrics require the embedded state $\rho_{\text{emb}}(t; \varepsilon)$ constructed from phase-space or soft-membership data (Section 2.3). If only the symbol sequence $\{S_n\}$ is available, the off-diagonal element $c(\varepsilon)$ cannot be measured, and diagnostic tools must rely on diagonal quantities: symbol entropy, likelihood-ratio tests, run-length distributions (Section 4), and windowed stationarity checks. Purity and fidelity are most informative when phase-space data permit estimation of both populations and boundary overlap.

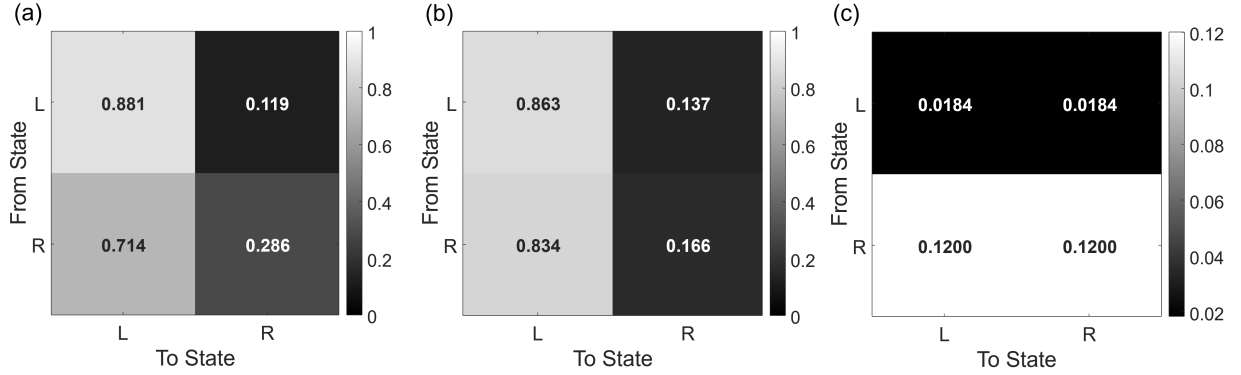


Figure 5: Chapman–Kolmogorov consistency test comparing empirical and predicted two-step transition probabilities. (a) Empirical two-step matrix $\hat{\mathbf{P}}^{(2)}$ estimated from symbol pairs separated by two periods. (b) Predicted two-step matrix $\hat{\mathbf{P}}^2$ computed by squaring the one-step matrix. (c) Element-wise discrepancy $|\hat{\mathbf{P}}^{(2)} - \hat{\mathbf{P}}^2|$ with Frobenius norm Δ_{CK} . Small discrepancies indicate Chapman–Kolmogorov consistency, validating the Markov property across time scales (Section 4). Parameters: $\alpha = 1.0$, $\beta = 1.0$, $\delta = 0.15$, $\gamma_0 = 0.3$, $\omega = 1.0$.

These tools are classical operational quantities, applied to classical measurements of coarse-grained occupancy statistics. They do not require quantum hardware; rather, they provide rigorous, interpretable diagnostics for model selection and uncertainty quantification.

Possible future roles for quantum-assisted analysis. If and when practical quantum processors become available for small systems (tens to hundreds of qubits), the ability to directly implement Lindblad propagators via jump-operator circuits offers an *alternative simulation pathway*. This would not provide computational speedup (classical matrix exponentiation is efficient for 2-state systems); rather, it would enable cross-platform validation of the model and exploration of very-high-dimensional extensions ($d \gg 10$) on quantum hardware. For the current focus (2-state and $d < 10$ systems), classical methods suffice.

8 Conclusion

We presented a Lindblad–Pauli framework for coarse-grained chaotic bistable dynamics, centered on a two-state embedding of Duffing left/right statistics into a 2×2 density matrix and a two-rate GKSL generator for inter-well switching. The framework yields closed-form solutions, an explicit Kraus representation, and a set of falsifiable diagnostics for the Markov assumptions implicit in a two-state reduction. A soft-partition embedding induces a Bloch half-disk state space and a coarse-graining diagnostic $c(\varepsilon)$ that quantifies partition fuzziness; this parameter characterizes the embedding geometry but is not a dynamical variable of the reduced model, which governs only population evolution from symbol observations.

When experimental diagnostics reveal deviations from first-order Markov behavior—such as second-order memory effects evidenced by G-test statistics with $p \ll 0.01$ —the framework extends naturally through state-space augmentation to 4×4 (or higher-dimensional) GKSL models. Importantly, the Chapman–Kolmogorov consistency test can still hold in such cases, confirming that the Markov property is satisfied at a higher order and that the GKSL formalism remains valid and applicable. This demonstrates that the framework is not rigidly tied to first-order models but provides a systematic, extensible approach to modeling coarse-grained dynamics with complete positivity guarantees.

A detailed numerical pipeline and figure/table templates were provided to support a companion computational validation study.

A Detailed derivation of the evolution equations

Notation. In this appendix we write ρ for ρ_{mod} to simplify notation.

This appendix provides a direct derivation of Theorem 3.1 for completeness.

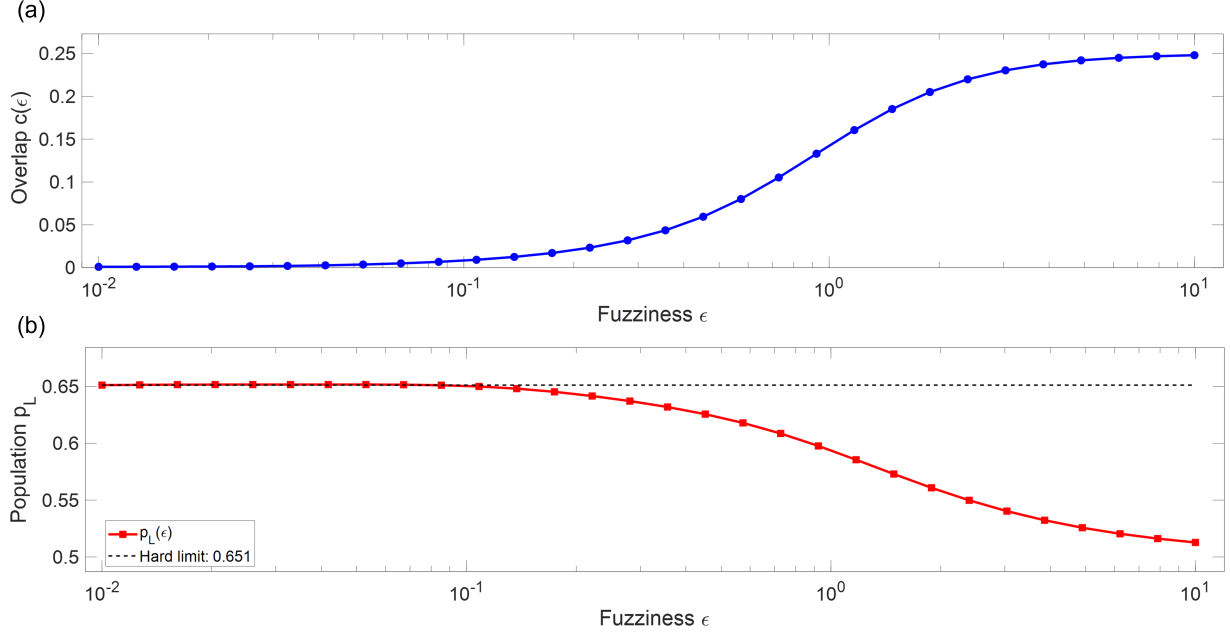


Figure 6: Overlap parameter $\hat{c}(\varepsilon)$ and population $p_L(\varepsilon)$ versus soft-partition fuzziness ε . (a) Overlap $\hat{c}(\varepsilon) = \langle \sqrt{w_L w_R} \rangle$ decreases toward zero as $\varepsilon \rightarrow 0^+$, demonstrating convergence to hard-partition limit (Proposition 2.8). (b) Left-well population $p_L(\varepsilon) = \langle w_L \rangle$ converges to the hard-partition value as $\varepsilon \rightarrow 0^+$ and varies with increased fuzziness. This quantifies the sensitivity of the embedded state $\rho_{\text{emb}}(\varepsilon)$ to the resolution parameter ε (Section 2.3). These diagnostics characterize how the embedding choice (controlled by ε) affects the coarse-grained state representation, but are *not* predicted by the GKSL dynamics, which governs only population evolution from symbol observations (Section 2.3). The GKSL steady state is diagonal ($\rho_{LR}^* = 0$, Theorem 3.4) because symbols contain no boundary-proximity information. Parameters: $\alpha = 1.0$, $\beta = 1.0$, $\delta = 0.15$, $\gamma_0 = 0.3$, $\omega = 1.0$.

Let $\rho = \begin{pmatrix} \rho_{LL} & \rho_{LR} \\ \rho_{RL} & \rho_{RR} \end{pmatrix}$. We evaluate the GKSL terms in (20) for the operators (21)–(24).

Hamiltonian term. With $H = -(\Delta E/2)\sigma_z$,

$$[H, \rho] = H\rho - \rho H = \begin{pmatrix} 0 & -\Delta E \rho_{LR} \\ +\Delta E \rho_{RL} & 0 \end{pmatrix},$$

hence

$$-\frac{i}{\hbar}[H, \rho] = \begin{pmatrix} 0 & +i\Omega \rho_{LR} \\ -i\Omega \rho_{RL} & 0 \end{pmatrix}.$$

Jump $L_+ = \sqrt{k_{LR}}\sigma_+$. Compute

$$L_+ \rho L_+^\dagger = k_{LR} \sigma_+ \rho \sigma_- = k_{LR} \begin{pmatrix} 0 & 0 \\ 0 & \rho_{LL} \end{pmatrix}, \quad L_+^\dagger L_+ = k_{LR} \sigma_- \sigma_+ = k_{LR} \begin{pmatrix} 1 & 0 \\ 0 & 0 \end{pmatrix}.$$

Thus

$$\mathcal{D}[L_+] \rho = L_+ \rho L_+^\dagger - \frac{1}{2} \{L_+^\dagger L_+, \rho\} = \begin{pmatrix} -k_{LR} \rho_{LL} & -\frac{k_{LR}}{2} \rho_{LR} \\ -\frac{k_{LR}}{2} \rho_{RL} & +k_{LR} \rho_{LL} \end{pmatrix}.$$

Jump $L_- = \sqrt{k_{RL}}\sigma_-$. Similarly,

$$\mathcal{D}[L_-] \rho = \begin{pmatrix} +k_{RL} \rho_{RR} & -\frac{k_{RL}}{2} \rho_{LR} \\ -\frac{k_{RL}}{2} \rho_{RL} & -k_{RL} \rho_{RR} \end{pmatrix}.$$

Dephasing $L_d = \sqrt{\kappa}\sigma_z$. Since $\sigma_z^2 = \mathbb{I}$,

$$\mathcal{D}[L_d] \rho = \kappa \sigma_z \rho \sigma_z - \kappa \rho = \begin{pmatrix} 0 & -2\kappa \rho_{LR} \\ -2\kappa \rho_{RL} & 0 \end{pmatrix}.$$

Combine terms. Summing Hamiltonian and dissipators gives

$$\dot{\rho}_{LL} = -k_{LR}\rho_{LL} + k_{RL}\rho_{RR}, \quad \dot{\rho}_{RR} = +k_{LR}\rho_{LL} - k_{RL}\rho_{RR},$$

and

$$\dot{\rho}_{LR} = i\Omega\rho_{LR} - \frac{k_{LR} + k_{RL}}{2}\rho_{LR} - 2\kappa\rho_{LR} = \left(i\Omega - \frac{\Gamma}{2} - 2\kappa\right)\rho_{LR},$$

which is Theorem 3.1.

B Proof details for the Kraus equivalence

Notation. We write ρ for ρ_{mod} throughout.

This appendix provides the explicit matrix-element computation for Theorem 4.9.

Write $\rho(0) = \begin{pmatrix} a & c \\ c^* & b \end{pmatrix}$ with $a + b = 1$. Let $\mathcal{E}_t(\rho) = \sum_{j=0}^3 E_j \rho E_j^\dagger$. Using (42)–(43) one finds

$$\begin{aligned} E_0 \rho E_0^\dagger &= p_L^* \begin{pmatrix} a & c\sqrt{1-\lambda} \\ c^*\sqrt{1-\lambda} & b(1-\lambda) \end{pmatrix}, \\ E_1 \rho E_1^\dagger &= p_L^* \begin{pmatrix} \lambda b & 0 \\ 0 & 0 \end{pmatrix}, \\ E_2 \rho E_2^\dagger &= p_R^* \begin{pmatrix} (1-\lambda)a & c\sqrt{1-\lambda} \\ c^*\sqrt{1-\lambda} & b \end{pmatrix}, \\ E_3 \rho E_3^\dagger &= p_R^* \begin{pmatrix} 0 & 0 \\ 0 & \lambda a \end{pmatrix}. \end{aligned}$$

Summing yields

$$(\mathcal{E}_t(\rho))_{LL} = (1-\lambda)a + \lambda p_L^*, \quad (\mathcal{E}_t(\rho))_{LR} = \sqrt{1-\lambda}c.$$

Next apply $\mathcal{Z}_t(\rho) = \sum_{a=0}^1 F_a \rho F_a^\dagger$ with (44). Since $F_0 \propto \mathbb{I}$ and $F_1 \propto \sigma_z$,

$$\mathcal{Z}_t(\rho) = \frac{1+\eta}{2}\rho + \frac{1-\eta}{2}\sigma_z \rho \sigma_z,$$

so diagonal entries are unchanged and $(\mathcal{Z}_t(\rho))_{LR} = \eta\rho_{LR}$. Finally, $\mathcal{U}_t(\rho) = U\rho U^\dagger$ preserves diagonal entries and multiplies ρ_{LR} by $e^{i\Omega t}$. Combining $\Lambda_t = \mathcal{U}_t \circ \mathcal{Z}_t \circ \mathcal{E}_t$ gives

$$\rho_{LL}(t) = (1-\lambda(t))\rho_{LL}(0) + \lambda(t)p_L^* = p_L^* + (\rho_{LL}(0) - p_L^*)e^{-\Gamma t},$$

since $1-\lambda(t) = e^{-\Gamma t}$, and

$$\rho_{LR}(t) = e^{i\Omega t} \eta(t) \sqrt{1-\lambda(t)} \rho_{LR}(0) = \rho_{LR}(0) \exp \left[\left(i\Omega - \frac{\Gamma}{2} - 2\kappa \right) t \right],$$

since $\eta(t) = e^{-2\kappa t}$ and $\sqrt{1-\lambda(t)} = e^{-\Gamma t/2}$. This reproduces (46)–(47).

C Why pure Hamiltonian evolution cannot model switching

This appendix formalizes why a purely Hamiltonian evolution does not change diagonal populations when H is diagonal in the $\{|L\rangle, |R\rangle\}$ basis.

Theorem C.1 (Diagonal Hamiltonians preserve diagonal populations). *Let $H = c_0\mathbb{I} + c_z\sigma_z$ and let $\rho = \text{diag}(p_L, p_R)$. Then the von Neumann equation $\dot{\rho} = -(i/\hbar)[H, \rho]$ gives $\dot{\rho} = 0$.*

Proof. Both H and ρ are diagonal matrices, hence they commute: $[H, \rho] = 0$. □

Remark C.2. Geometrically, $H \propto \sigma_z$ generates rotations about the Bloch z -axis. Diagonal states lie on that axis and are invariant under such rotations. Population transfer requires either off-diagonal Hamiltonian terms (σ_x, σ_y components) or dissipative jump terms (GKSL).

C.1 Non-Hermitian “dissipative Hamiltonians” lead to nonlinear dynamics

A common heuristic is to use $H_{\text{diss}} = H - iG$ with $G \succeq 0$, and then renormalize:

$$\rho(t) = \frac{e^{-iH_{\text{diss}}t/\hbar} \rho(0) e^{+iH_{\text{diss}}^\dagger t/\hbar}}{\text{Tr}(\dots)}.$$

This yields a nonlinear evolution.

Theorem C.3 (Renormalized non-Hermitian evolution is nonlinear). *The above normalized evolution satisfies*

$$\frac{d\rho}{dt} = -\frac{i}{\hbar}[H, \rho] - \frac{1}{\hbar}\{G, \rho\} + \frac{2}{\hbar}\text{Tr}(G\rho)\rho, \quad (52)$$

whose last term is quadratic in ρ .

Proof. Differentiate the unnormalized $\tilde{\rho}(t) = e^{-iH_{\text{diss}}t/\hbar} \rho(0) e^{+iH_{\text{diss}}^\dagger t/\hbar}$ and apply the quotient rule to $\rho = \tilde{\rho} / \text{Tr}(\tilde{\rho})$. \square

Remark C.4. Such normalized non-Hermitian dynamics is not a linear CPTP map on density matrices; it corresponds to a conditional (post-selected) “no-jump” evolution in quantum-trajectory language, not an unconditional dissipative dynamics.

D Symmetry and the energy splitting parameter

In symmetric Duffing parameters (no bias; symmetric potential), one typically expects equal long-time occupations and no meaningful energy splitting between wells. We record a simple symmetry argument.

For the symmetric Duffing oscillator with potential $V(x) = -\alpha x^2/2 + \beta x^4/4$ (which satisfies $V(-x) = V(x)$ for any $\alpha, \beta > 0$), the wells centered at $x = \pm\sqrt{\alpha/\beta}$ have equal depths, implying $\Delta E = 0$. This yields $\Omega = 0$ throughout, ensuring the Bloch half-disk geometry remains closed under GKSL evolution. Asymmetric forcing or potential bias would break this symmetry and introduce nonzero Ω .

Proposition D.1 (Parity symmetry of the standard Duffing potential). *For $V(x) = -(\alpha/2)x^2 + (\beta/4)x^4$, one has $V(-x) = V(x)$.*

Definition D.2 (Conditional energy averages). Define

$$\langle E \rangle_L = \frac{1}{|\Omega_L|} \int_{\Omega_L} E(t) dt, \quad \Omega_L = \{t : x(t) < 0\}, \quad \langle E \rangle_R = \frac{1}{|\Omega_R|} \int_{\Omega_R} E(t) dt, \quad \Omega_R = \{t : x(t) > 0\},$$

where $E(t) = \frac{1}{2}\dot{x}(t)^2 + V(x(t))$.

Theorem D.3 (Symmetry implies zero conditional energy splitting). *If the stationary statistics of (x, \dot{x}) are symmetric under $(x, \dot{x}) \mapsto (-x, -\dot{x})$, then $\langle E \rangle_L = \langle E \rangle_R$ and thus any conditional energy splitting vanishes.*

Proof. Since $E(-x, -\dot{x}) = E(x, \dot{x})$ and the parity map exchanges the events $\{x < 0\}$ and $\{x > 0\}$ under the symmetry assumption, the conditional distributions are mapped into each other and the conditional expectations coincide. \square

Remark D.4 (Finite-time ergodicity and experimental validation). Theorem D.3 assumes that the stationary statistics are fully symmetric and that the system has reached ergodic equilibrium. In practice, finite-time numerical simulations may not fully explore the attractor, particularly in chaotic systems with complex basin structures or slow mixing. Consequently, empirical estimates of $\langle E \rangle_L$ and $\langle E \rangle_R$ may exhibit small asymmetries that are artifacts of incomplete sampling rather than genuine physical asymmetry. When experimental data suggest nonzero energy splitting or asymmetric dwell-time statistics (see Section 4), it is prudent to verify convergence by extending the simulation duration and checking stability of statistical estimates, test multiple initial conditions to assess sensitivity to transient dynamics, and consider higher-resolution diagnostics (e.g., phase-space density plots on the Poincaré section) to confirm whether the observed asymmetry is systematic or sampling-related. These checks help distinguish true symmetry breaking from finite-time numerical artifacts.

E Summary of key formulas

For convenience we collect a few formulas used throughout the paper. We distinguish ρ_{emb} (embedded state from phase-space data) and ρ_{mod} (model state governed by GKSL).

Embedded state (from phase-space data).

Quantity	Formula
Definition	$\rho_{\text{emb}}(t; \varepsilon, \Delta) = \int \mu_t(z) \psi(z)\rangle \langle \psi(z) dz$
Off-diagonal element	$[\rho_{\text{emb}}]_{LR} = c(t; \varepsilon) = \langle \sqrt{w_L w_R} \rangle$
Half-disk constraint	$c^2 \leq p_L(1 - p_L)$, with $m_x = 2c \geq 0$ and $m_x^2 + m_z^2 \leq 1$

Model state (GKSL dynamics).

Quantity	Formula
GKSL equation	$\dot{\rho}_{\text{mod}} = -(i/\hbar)[H, \rho_{\text{mod}}] + \sum_k (L_k \rho_{\text{mod}} L_k^\dagger - \frac{1}{2}\{L_k^\dagger L_k, \rho_{\text{mod}}\})$
Jump operators	$L_+ = \sqrt{k_{LR}} \sigma_+, L_- = \sqrt{k_{RL}} \sigma_-$
Relaxation rate	$\Gamma = k_{LR} + k_{RL}$
Steady state	$p_L^* = k_{RL}/\Gamma, p_R^* = k_{LR}/\Gamma; [\rho_{\text{mod}}^*]_{LR} = 0$
Population solution	$p_L(t) = p_L^* + (p_0 - p_L^*)e^{-\Gamma t}$
Off-diagonal solution	$[\rho_{\text{mod}}]_{LR}(t) = [\rho_{\text{mod}}]_{LR}(0)e^{(i\Omega - \Gamma/2 - 2\kappa)t}$
Discrete-time P_{ij}	$P_{LR} = p_R^*(1 - e^{-\Gamma T}), P_{RL} = p_L^*(1 - e^{-\Gamma T})$
Rate inversion	$\hat{\Gamma} = -(1/T) \ln(1 - \hat{P}_{LR} - \hat{P}_{RL})$, then (39)

F Notation and terminology

This appendix provides a comprehensive reference for all key symbols, operators, and terminology used throughout the paper, organized by category. For first appearance, we refer to the relevant equation, definition, theorem, or section.

F.1 Physical system and observables

Symbol	Description	First appearance
x	Displacement of Duffing oscillator	Eq. (1)
\dot{x}	Velocity of Duffing oscillator	Eq. (1)
δ	Damping coefficient ($\delta > 0$)	Eq. (1)
α	Linear restoring force coefficient ($\alpha > 0$)	Eq. (1)
β	Cubic nonlinearity coefficient ($\beta > 0$)	Eq. (1)
γ_0	Forcing amplitude	Eq. (1)
ω	Forcing frequency	Eq. (1)
$V(x)$	Potential energy function	Eq. (2)
x_\pm	Stable equilibria at $\pm \sqrt{\alpha/\beta}$	Eq. (2)
ΔV	Barrier height $\alpha^2/(4\beta)$	Eq. (2)
D	Noise intensity (stochastic extension)	Eq. (3)
T	Forcing period $2\pi/\omega$	Sec. 2
t_n	Sampling times nT (Poincaré section)	Sec. 2
z	Phase-space point (x, \dot{x}) on Poincaré section	Def. 2.4
$E(t)$	Total energy $\frac{1}{2}\dot{x}^2 + V(x)$	App. D

F.2 Symbol sequences and coarse-graining

Symbol	Description	First appearance
S_n	Binary symbol at time t_n ($S_n \in \{L, R\}$)	Def. 2.2
$\{S_n\}$	Discrete-time symbol sequence	Def. 2.2
L	Left-well symbol (typically $x < 0$)	Def. 2.2
R	Right-well symbol (typically $x > 0$)	Def. 2.2
$g(z)$	Signed boundary function (separatrix approximation)	Def. 2.4
ε	Fuzziness parameter for soft partition ($\varepsilon > 0$)	Def. 2.4
$w_L(z)$	Soft membership function for left well	Eq. (10)
$w_R(z)$	Soft membership function for right well ($w_R = 1 - w_L$)	Eq. (10)
$\mu_t(z)$	Phase-space probability density or empirical measure	Def. 2.7
Δ	Window length for empirical measure	Def. 2.9
N	Number of Poincaré samples	Sec. 5

F.3 Quantum-inspired two-state representation

Symbol	Description	First appearance
$ L\rangle$	Computational basis state for left well	Sec. 2.3
$ R\rangle$	Computational basis state for right well	Sec. 2.3
$ \psi(z)\rangle$	Pointwise embedded two-state vector	Eq. (11)
ρ	Generic 2×2 density matrix	Eq. (8)
ρ_{emb}	Embedded state from phase-space data	Eq. (12)
ρ_{mod}	Model state governed by GKSL dynamics	Sec. 2.7
ρ_{LL}	Diagonal element (left-well population)	Thm. 3.1
ρ_{RR}	Diagonal element (right-well population)	Thm. 3.1
ρ_{LR}	Off-diagonal element (coherence)	Thm. 3.1
ρ_{RL}	Off-diagonal element ($\rho_{RL} = \rho_{LR}^*$)	Thm. 3.1
ρ^*	Steady-state density matrix	Thm. 3.4
$p_L(t)$	Population in left well at time t	Prop. 2.8
$p_R(t)$	Population in right well at time t ($p_R = 1 - p_L$)	Prop. 2.8
p_L^*	Steady-state left-well population k_{RL}/Γ	Thm. 3.4
p_R^*	Steady-state right-well population k_{LR}/Γ	Thm. 3.4
$c(t)$	Overlap parameter $\langle \sqrt{w_L w_R} \rangle$	Prop. 2.8
$c(\varepsilon)$	Overlap parameter as function of fuzziness	Eq. (48)
$\hat{c}(\varepsilon)$	Empirical estimate of overlap parameter	Eq. (48)

F.4 Pauli matrices and Bloch representation

Symbol	Description	First appearance
σ_x	Pauli-X matrix (bit-flip)	Eq. (6)
σ_y	Pauli-Y matrix	Eq. (6)
σ_z	Pauli-Z matrix (population difference)	Eq. (6)
σ_+	Raising operator $ R\rangle\langle L $	Eq. (7)
σ_-	Lowering operator $ L\rangle\langle R $	Eq. (7)
\mathbf{m}	Bloch vector (m_x, m_y, m_z)	Eq. (8)
m_x	Bloch x -component ($m_x = 2c$ for real states)	Eq. (8)
m_y	Bloch y -component ($m_y = 0$ for symmetric case)	Eq. (8)
m_z	Bloch z -component ($m_z = p_L - p_R = 2p_L - 1$)	Eq. (8)
m_z^*	Steady-state z -component $(k_{RL} - k_{LR})/\Gamma$	Eq. (31)
\mathbb{I}	2×2 identity matrix	Eq. (8)

F.5 GKSL generator and rates

Symbol	Description	First appearance
H	Hamiltonian operator $-(\Delta E/2)\sigma_z$	Eq. (21)
ΔE	Energy splitting between wells	Eq. (21)
Ω	Rabi-like frequency $\Delta E/\hbar$	Def. 2.17
\hbar	Reduced Planck constant (formal parameter)	Eq. (20)
L_k	Generic Lindblad jump operator	Eq. (20)
L_+	Jump operator $\sqrt{k_{LR}}\sigma_+$ (L \rightarrow R)	Eq. (22)
L_-	Jump operator $\sqrt{k_{RL}}\sigma_-$ (R \rightarrow L)	Eq. (23)
L_d	Dephasing operator $\sqrt{\kappa}\sigma_z$	Eq. (24)
k_{LR}	Switching rate from left to right well	Def. 2.17
k_{RL}	Switching rate from right to left well	Def. 2.17
Γ	Total relaxation rate $k_{LR} + k_{RL}$	Thm. 3.1
κ	Pure dephasing rate	Eq. (24)
τ_{rel}	Population relaxation time $1/\Gamma$	Sec. 3.2
τ_{off}	Off-diagonal decay time $1/(\Gamma/2 + 2\kappa)$	Sec. 3.2
$\hat{\Gamma}$	Estimated total relaxation rate	Eq. (38)
\hat{k}_{LR}	Estimated L \rightarrow R switching rate	Eq. (39)
\hat{k}_{RL}	Estimated R \rightarrow L switching rate	Eq. (39)

E.6 Discrete-time transition probabilities

Symbol	Description	First appearance
\mathbf{P}	One-step transition probability matrix	Eq. (36)
P_{ij}	Transition probability from state i to state j	Eq. (37)
P_{LR}	One-step transition probability L \rightarrow R	Eq. (37)
P_{RL}	One-step transition probability R \rightarrow L	Eq. (37)
\hat{P}_{ij}	Empirical estimate of P_{ij}	Sec. 4
$\hat{\mathbf{P}}$	Empirical one-step transition matrix	Sec. 4
$\hat{\mathbf{P}}^{(2)}$	Empirical two-step transition matrix	Sec. 4
N_{ij}	Transition count from state i to state j	Sec. 4
N_{kij}	Second-order transition count $k \rightarrow i \rightarrow j$	Sec. 4
$p_L^{(n)}$	Left-well population at discrete time n	Eq. (35)

E.7 Kraus operators

Symbol	Description	First appearance
$K_\ell(t)$	Generic Kraus operator	Sec. 4.7
Λ_t	CPTP map $\rho(0) \mapsto \rho(t)$	Sec. 4.7
$\lambda(t)$	Relaxation parameter $1 - e^{-\Gamma t}$	Sec. 4.7
$\eta(t)$	Dephasing parameter $e^{-2\kappa t}$	Sec. 4.7
$U(t)$	Unitary evolution operator $e^{-iHt/\hbar}$	Sec. 4.7
$E_j(t)$	GAD (generalized amplitude damping) Kraus operators	Eq. (42), (43)
$F_a(t)$	Phase-damping Kraus operators	Eq. (44)
$M_{aj}(t)$	Composite Kraus operators $U(t)F_a(t)E_j(t)$	Eq. (45)

F.8 Diagnostic tests and statistics

Symbol	Description	First appearance
G	G-test statistic (likelihood ratio)	Eq. (40)
$\hat{P}_{ij k}$	Conditional transition probability given previous state k	Sec. 4
Δ_{CK}	Chapman-Kolmogorov discrepancy $\ \hat{\mathbf{P}}^{(2)} - \hat{\mathbf{P}}^2\ _F$	Sec. 4
p_{CK}	Chapman-Kolmogorov test p -value	Table 1
R_L	Run length (dwell time) in left well	Sec. 4
R_R	Run length (dwell time) in right well	Sec. 4
W	Number of windows for stationarity test	Sec. 4
$\hat{P}_{ij}^{(w)}$	Transition probability in window w	Sec. 4
B	Number of bootstrap replicates	Sec. 6.2
ℓ	Block length for block bootstrap	Eq. (49)
τ_{int}	Integrated autocorrelation time	Sec. 6.2
df	Degrees of freedom for χ^2 test	Eq. (41)

F.9 Acronyms and abbreviations

Acronym	Meaning
GKSL	Gorini-Kossakowski-Sudarshan-Lindblad (master equation)
CPTP	Completely Positive and Trace-Preserving (quantum channel)
GAD	Generalized Amplitude Damping (quantum channel)
ODE	Ordinary Differential Equation
SDE	Stochastic Differential Equation

F.10 Mathematical operators and notation

Symbol	Description	First appearance
Tr	Trace operator	Sec. 2 (custom command)
d	Differential operator (upright d)	Sec. 2 (custom command)
$ \cdot\rangle$	Ket (column) vector in Dirac notation	Sec. 2 (custom command)
$\langle\cdot $	Bra (row) vector in Dirac notation	Sec. 2 (custom command)
$ \cdot\rangle\langle\cdot $	Outer product $ \cdot\rangle\langle\cdot $	Sec. 2 (custom command)
$\langle\cdot\rangle$	Expectation value	Sec. 2 (custom command)
$\ \cdot\ $	Norm (default: Euclidean or Frobenius)	Sec. 2 (custom command)
$\ \cdot\ _F$	Frobenius norm	Sec. 4
$[A, B]$	Commutator $AB - BA$	Eq. (20)
$\{A, B\}$	Anticommutator $AB + BA$	Eq. (20)
A^\dagger	Hermitian adjoint (conjugate transpose)	Eq. (20)
A^*	Complex conjugate or steady-state value (context-dependent)	Throughout

References

- [1] F. C. Moon. *Chaotic Vibrations: An Introduction for Applied Scientists and Engineers*. Wiley, 1987.
- [2] J. Guckenheimer and P. Holmes. *Nonlinear Oscillations, Dynamical Systems, and Bifurcations of Vector Fields*. Springer, 1983.
- [3] B. McNamara and K. Wiesenfeld. Theory of stochastic resonance. *Physical Review A*, 39:4854–4869, 1989.
- [4] L. Gammaitoni, P. Hänggi, P. Jung, and F. Marchesoni. Stochastic resonance. *Reviews of Modern Physics*, 70:223–287, 1998.
- [5] G. Lindblad. On the generators of quantum dynamical semigroups. *Communications in Mathematical Physics*, 48:119–130, 1976.
- [6] V. Gorini, A. Kossakowski, and E. C. G. Sudarshan. Completely positive dynamical semigroups of N -level systems. *Journal of Mathematical Physics*, 17:821–825, 1976.
- [7] H.-P. Breuer and F. Petruccione. *The Theory of Open Quantum Systems*. Oxford University Press, 2002.
- [8] F. Nathan and M. S. Rudner. Universal Lindblad equation for open quantum systems. *Physical Review B*, 102:115109, 2020.
- [9] K. Kawabata, A. Kulkarni, J. Li, T. Numasawa, and S. Ryu. Symmetry of open quantum systems: Classification of dissipative quantum chaos. *PRX Quantum*, 4:030328, 2023.
- [10] S. Lange and C. Timm. Random-matrix theory for the Lindblad master equation. *Chaos: An Interdisciplinary Journal of Nonlinear Science*, 31:023101, 2021.
- [11] A. S. Trushechkin et al. Quantum master equation for many-body systems based on the Lieb-Robinson bound. *Physical Review B*, 111:184311, 2024.
- [12] J. Galkowski, M. Zworski, and Z. Huang. Classical–quantum correspondence in Lindblad evolution. *Journal of Mathematical Physics*, 66:091503, 2025.

- [13] W. H. Zurek. Decoherence, einselection, and the quantum origins of the classical. *Reviews of Modern Physics*, 75:715–775, 2003.
- [14] F. Hernández, D. Ranard, and C. J. Riedel. Classical correspondence beyond the Ehrenfest time for open quantum systems with general Lindbladians. *Communications in Mathematical Physics*, 406:4, 2025.
- [15] J. D. Whitfield, C. A. Rodríguez-Rosario, and A. Aspuru-Guzik. Quantum stochastic walks: A generalization of classical random walks and quantum walks. *Physical Review A*, 81:022323, 2010.
- [16] A. Anand, K. Bharti, P. Batra, G. Bulnes-Cuetara, S. Fritzsche, V. Kabel, E. Solano, A. R. U. Devi, and S. Varma. Simulating quantum chaos on a quantum computer. *Scientific Reports*, 14:26890, 2024.
- [17] N. F. Berthussen, T. V. Trevisan, and P. P. Orth. Optimal conversion from classical to quantum randomness via quantum chaos. *Physical Review Letters*, 134:180403, 2025.
- [18] S. L. Brunton, M. Budišić, E. Kaiser, and J. N. Kutz. Modern Koopman theory for dynamical systems. *SIAM Review*, 64:229–340, 2022.
- [19] Q. Li, F. Dietrich, E. M. Bollt, and I. G. Kevrekidis. Extended dynamic mode decomposition with dictionary learning: A data-driven adaptive spectral decomposition of the Koopman operator. *Chaos: An Interdisciplinary Journal of Nonlinear Science*, 27:103111, 2017.
- [20] A. Mauroy, Y. Susuki, and I. Mezić. Koopman operator and its approximations for systems with symmetries. *Chaos: An Interdisciplinary Journal of Nonlinear Science*, 29:093128, 2019.
- [21] J. Barrett. Information processing in generalized probabilistic theories. *Physical Review A*, 75:032304, 2007.
- [22] P. Janotta and H. Hinrichsen. Generalized probability theories: what determines the structure of quantum theory? *Journal of Physics A: Mathematical and Theoretical*, 47:323001, 2014.
- [23] D. C. Brody and L. P. Hughston. Geometric quantum mechanics. *Journal of Geometry and Physics*, 38(1):19–53, 2001.
- [24] S.-I. Amari. *Information Geometry and Its Applications*. Springer, 2016.
- [25] T. Kailath. The divergence and Bhattacharyya distance measures in signal selection. *IEEE Transactions on Communication Technology*, 15(1):52–60, 1967.
- [26] R. Killick, P. Fearnhead, and I. A. Eckley. Optimal detection of changepoints with a linear computational cost. *Journal of the American Statistical Association*, 107:1590–1598, 2012.
- [27] D. N. Politis and J. P. Romano. The stationary bootstrap. *Journal of the American Statistical Association*, 89:1303–1313, 1994.
- [28] S. N. Lahiri. Theoretical comparisons of block bootstrap schemes. *Journal of the American Statistical Association*, 94:688–700, 1999.